JOURNAL OF AGRICULTURAL AND FOOD CHEMISTRY

pubs.acs.org/JAFC Article

Camel-Milk-Derived Extracellular Vesicles Mitigate High-Fat-Diet-Induced Obesity by Enhancing Thermogenesis and Modulating Lipid Metabolism in Mice

Shuai Wang,[⊥] Shuting Liu,[⊥] Ting He, Huanming Shen, Chunli Mo, Yu Zhu, Wenlong Xie, Boan Li, Weihua Li,[*] and Jian Zhang[*]

Cite This: *J. Agric. Food Chem.* 2025, 73, 21404−21421 Read Online

ACCESS | Metrics & More | Article Recommendations | Supporting Information

ABSTRACT: Obesity is a significant global health concern linked to chronic diseases, with the thermogenic capacity of brown adipose tissue (BAT) being crucial for obesity treatment. This study investigates the potential of camel-milk-derived extracellular vesicles (mEVs) in mitigating high-fat-diet-induced obesity and metabolic dysfunction in mice. Our results show that oral administration of mEVs significantly reduces body fat percentage and lipid accumulation while lowering serum triglycerides, free fatty acids, and cholesterol levels. Furthermore, mEVs enhance thermogenic capacity during cold exposure, indicated by increased oxygen consumption and heat production. RNA sequencing of BAT reveals that mEVs upregulate thermogenesis and oxidative phosphorylation-related genes. Additionally, mEVs positively modulate the gut microbiota by promoting beneficial taxa and partially restoring short-chain fatty acid production. Consequently, these results suggest mEVs enhance BAT thermogenesis and improve metabolic health, offering a potential therapeutic strategy for obesity and related disorders.

KEYWORDS: *Camel-milk-derived extracellular vesicles, Obesity, Thermogenesis, Lipid Metabolism, Gut Microbiota*

INTRODUCTION

Obesity has become a significant global health concern, serving as a critical risk factor for the development of numerous chronic diseases, including insulin resistance, type 2 diabetes (T2D), hypertension, and atherosclerosis, all of which constitute components of metabolic syndrome.[1,2] This condition arises from a persistent imbalance between energy intake and expenditure, leading to excess energy storage in white adipose tissue (WAT).[3] In obese patients, adipose tissue releases inflammatory factors, such as tumor necrosis factor-alpha (TNF-α), interleukin-1 beta (IL-1β), and interleukin-6 (IL-6), which promote the proliferation of M1 macrophages.[4,5] These macrophages, in turn, stimulate adipose tissue to release additional inflammatory factors through NF-κB signaling pathway.[6] In addition to white adipose tissue, adipose tissue encompasses beige adipose tissue and brown adipose tissue (BAT), both of which exhibit high expression levels of uncoupling protein 1 (Ucp1).[7] Beige adipose tissue is a distinct type of adipocyte that develops within white adipose tissue and has the capacity to dissipate energy as heat in response to cold stimulation.

BAT is a highly metabolically active tissue primarily responsible for nonshivering thermogenesis.[8] Transcriptional regulators, including SRY-related High Mobility Group box transcription factor 4 (SOX4), Early B-cell factor 2 (EBF2), and PR-domain containing protein 16 (PRDM16), play key roles in the development and function of BAT.[9] EBF2 is a crucial transcriptional regulator for brown adipocyte differentiation and thermogenic function, promoting thermogenic gene expression and maintaining core temperature in BAT.[10,11] Our previous research indicates that SOX4 is an essential upstream regulator of EBF2, promoting brown adipose tissue development and thermogenic function by enhancing EBF2 transcription and thermogenic gene expression.[9] Brown adipocytes are rich in mitochondria and contain multiple lipid droplets, allowing them to effectively utilize fatty acids and glucose to produce heat.[12] Mitochondria are vital for BAT thermogenesis, with Peroxisome Proliferator-Activated Receptor Gamma Coactivator 1-alpha (PGC-1α) regulating mitochondrial biogenesis and function.[13] The loss of PGC-1α reduces mitochondrial density and energy expenditure, leading to cold sensitivity and obesity in mice.[14] Recent investigations have elucidated the essential role of BAT in human health, highlighting a significant correlation between increased BAT activity and reductions in body weight, alongside enhancements in metabolic parameters.[15,16] These findings suggest that the promotion of BAT thermogenic function could serve as a viable strategy for combating obesity and its associated metabolic disorders. By targeting BAT, we may not only mitigate the prevalence of obesity but also improve overall health outcomes, thus underscoring the importance of BAT in metabolic regulation.[17,18]

Received: February 27, 2025
Revised: August 6, 2025
Accepted: August 6, 2025
Published: August 14, 2025

Milk-derived exosomes are nanoscale extracellular vesicles secreted by mammary cells, characterized by their rich composition of proteins, lipids, and nucleic acids, conferring remarkable biocompatibility and stability.[19,20] These exosomes exhibit significant anti-inflammatory properties, effectively modulating immune cell functions and inhibiting the production of pro-inflammatory factors, thus mitigating tissue damage and chronic inflammation.[21] Concurrently, milk-derived exosomes possess potent antioxidant capabilities, enabling them to scavenge free radicals and reduce oxidative stress, which is crucial for cellular health and may have implications for antiaging therapies.[22] Furthermore, their role in promoting wound healing and tissue regeneration, particularly in metabolic disorders, underscores their therapeutic potential.[23] Notably, milk-derived exosomes demonstrate the ability to modulate gut microbiota composition, which holds therapeutic potential for improving metabolic disorders such as obesity and insulin resistance through the restoration of microbial balance and enhancement of gut barrier integrity.[24] However, despite these multifaceted benefits, a critical gap exists in the exploration of milk-derived exosomes within the context of obesity, highlighting the need for further research to elucidate their potential applications in this pressing health challenge.

Camel milk, due to its high nutritional value and unique health benefits, has gradually become a focal point of global research and market attention.[25] In this study, camel-milk-derived extracellular vesicles (mEVs) were orally administered in conjunction with high-fat feeding to evaluate their role in mitigating high-fat-induced obesity and metabolic dysfunction in mice. The oral administration of mEVs effectively countered high-fat-induced obesity, significantly reducing body fat percentage, adipose tissue mass, and lipid droplet accumulation, while also lowering serum triglycerides, free fatty acids, and total cholesterol levels. Cold exposure experiments revealed that mEV-treated mice maintained better thermoregulation, with increased oxygen consumption and heat production compared to controls. RNA sequencing of BAT demonstrated that mEVs feeding upregulated thermogenesis and oxidative phosphorylation-related genes, while downregulating lipogenesis genes. mEVs also modulate the gut microbiota composition by promoting beneficial taxa and reducing harmful ones. This intervention partially restores short-chain fatty acid (SCFA) production and reverses dysbiosis induced by a high-fat diet. Mechanistically, oral administration of mEVs activated the expression of SOX4 and EBF2 in BAT, thereby enhancing thermogenesis and alleviating high-fat-induced obesity.

MATERIALS AND METHODS

Vesicle Isolation. The protocol for isolating small cell-derived extracellular vesicles (EVs) from camel milk was adapted from Abdelnaser et al. (2025) and was appropriately modified.[26] Briefly, commercial pasteurized skimmed camel milk (200 mL) was first centrifuged at 13,200 × *g* for 30 min at 4 °C to remove somatic cells and debris, with the supernatant retained. The supernatant (120 mL) was then mixed with an equal volume of 0.25 M EDTA (pH = 7) and incubated on ice for 15 min to remove casein. Following this, ultracentrifugation was performed at 100,000 × *g* for 1 h at 4 °C to eliminate fat globules and larger EVs, yielding a new supernatant. The supernatant was then subjected to further ultracentrifugation at 120,000 × *g* for 90 min at 4 °C to pellet the vesicles (Umibio, Cat#UR90422). The vesicle pellet was washed twice with 0.01% sodium azide in PBS and resuspended in 500 μL PBS. The final suspension was filtered through a 0.22 μm membrane filter (Bioland, Cat#CS05-040). The resulting filtrate was either stored at −20 °C for long-term storage or used immediately for subsequent experiments at 4 °C. To evaluate the isolation efficiency, the expression of CD81 and TSG101 was detected. Additionally, nanoparticle tracking analysis (NTA) or transmission electron microscopy (TEM) was employed to confirm the successful isolation of extracellular vesicles from camel milk.[26]

Animal Experiment Design. The animal experiments conducted in this study were approved by the Institutional Animal Care and Research Advisory Committee of Xiamen University and received approval under Permit Number: XMULAC20230105. Mice were housed in colony cages under controlled environmental conditions, with temperatures maintained between 22 and 24 °C, humidity levels between 50 and 60%, and a 12-h light/dark cycle starting at 7:00 am. All animals used were age-matched male C57BL/6 mice, with specific ages noted in the figure legends. Wild-type (WT) mice were sourced from the Shanghai Model Organisms Center. *Myf5-Cre Sox4$^{f/f}$* mice (referred to as *Sox4-KO*) were generated by crossing *Sox4$^{f/f}$* mice with *Myf5-Cre* mice (GemPharmatech Company, Nanjing, China). Genotyping was performed using the Taq MasterMix (CWBIO, Cat#CW0690H; Shandong Sparkjade Biotechnology, Cat#AD0104), with the genotyping primers provided in Supplemental Table 1.

Both the high-fat diet and standard chow diet were supplied by Readydietech Co., Ltd. (Shenzhen, P.R. China) and Jiangsu Xietong Pharmaceutical Bioengineering Co., Ltd. The standard chow diet consisted of 67.4% carbohydrates, 20.6% protein, and 12% fat, whereas the high-fat diet contained 20% carbohydrates, 20% protein, and 60% fat by caloric content.

To investigate the effect of vesicles on body weight in mice, the animals were divided into five groups: normal feeding (NCD), high-fat feeding (HFD), and high-fat feeding combined with oral administration of low, medium, or high concentrations of vesicles (referred to as LV, MV, HV). The HFD group had ad libitum access to a high-fat diet, while the vesicle doses for the LV, MV, and HV groups were based on the study by Gao et al, with daily oral administration of 1 mg/kg, 3 mg/kg or 5 mg/kg of vesicles, respectively.[27] Additionally, the feeding regimen and body weight were carefully monitored throughout the experiment to ensure consistent conditions and reliable results. At the end of the experiment, the mice were humanely euthanized by administering a lethal dose of isoflurane anesthesia, followed by cervical dislocation to ensure a rapid and painless death. Subsequently, the following samples were collected: BAT for transcriptomic analysis, which was rapidly frozen in liquid nitrogen and stored at −80 °C; cecal contents for gut microbiota and short-chain fatty acid analysis, stored at −80 °C; blood serum, separated after centrifugation, for lipid profile analysis, also stored at −80 °C; adipose tissues including inguinal WAT (iWAT) and gonadal WAT (gWAT) and liver, fixed in 4% paraformaldehyde for subsequent histological analysis.

Serum Analysis. The serum samples were carefully removed from −80 °C and slowly thawed at room temperature for analysis. Triglyceride (TG), total cholesterol (T-CHO), alanine transaminase (ALT), aspartate transaminase (AST) and free fatty acid (FFA) levels were measured using the TG assay kit, T-CHO assay kit (Nanjing Jiancheng Bioengineering Institute), ALT assay kit, AST assay kit (Shanghai Jinma Laboratory Equipment co., LTD), and the free fatty acid assay kit (Bioswamp), respectively, following the manufacturer's protocols. Briefly, serum samples were incubated with specific reagents provided in the kits, and absorbance was measured at appropriate wavelengths using a microplate reader. The concentrations of TG, T-CHO, AST, ALT and FFA in the serum were determined based on standard curves generated from known concentrations of standards provided in the kits. The measurements were carried out in triplicate for each sample to ensure accuracy and reproducibility.

Serum Glucose Analysis. The blood samples were collected from experimental animals via eyeball. Serum was separated by centrifugation at 3,000 rpm for 15 min at 4 °C. Glucose concentration was determined using a glucose assay kit (Beyotime, Cat#S0202S)

https://doi.org/10.1021/acs.jafc.5c02577
J. Agric. Food Chem. 2025, 73, 21404−21421

following the manufacturer's instructions. Briefly, glucose oxidase catalyzes glucose oxidation, producing hydrogen peroxide, which reacts with a chromogenic reagent. Absorbance was measured at 540 nm, and serum glucose levels were calculated from a standard curve.

Body-Composition Analysis. The mice were carefully restrained using the designated tool to minimize movement and then positioned in the body composition analyzer for measurement. Body composition analysis, including the assessment of fat and lean mass, was performed using the Echo MRI system (Echo Medical Systems, model 100H), which offered noninvasive and accurate measurements of the body composition of the animals.

Metabolic Cage Study. Prior to the initiation of this study, mice were individually housed at a temperature of 22 °C for a duration of 1 week, followed by a 2-day period of acclimation to metabolic cages. The TSE-Phenomaster System was utilized to precisely monitor a range of parameters, such as food consumption, body weight, oxygen uptake, heat production, and ambulatory movements.

Immunohistochemistry and Immunofluorescence. For H&E staining, the adipose tissue and liver from mice were harvested and fixed in 4% paraformaldehyde (PFA) at room temperature for 12 h. Following fixation, the tissues were dehydrated through an ethanol gradient, embedded in paraffin, and sectioned to a thickness of 3 μm. The tissue sections were subsequently stained using the H&E Staining Kit (Wanleibio, Cat#WLA051a; Solarbio, Cat#G1106) according to the manufacturer's protocol.

For immunofluorescence of BAT, antigen retrieval was carried out using an antigen retrieval solution (Keygen BioTECH, Cat#KGC3110). The slides were incubated with 3% FBS (AMOBIO, Cat#FBSAB001) and 0.1% Triton X-100 (HUAYUN, Cat#SHB50396) in PBS (Pricella, Cat#PB180327) for 1 h at room temperature. The solution was filtered through a 0.22 μm filter head prior to use (BDBIO, Cat#H601014). After blocking, the slides were incubated with primary antibodies: anti-UCP1 (Abclonal, Cat#A5857) at a dilution of 1:100, and anti-AGT (Promab, Cat#20360) at a dilution of 1:100. The sections were then incubated with appropriate secondary antibodies conjugated to fluorescent dyes (EpiZyme, Cat#LF107; ZCIBIO Technology, Cat#ZC-G2129) for 1 h at room temperature in the dark. To counterstain the nuclei, the slides were treated with 5 μg/mL DAPI (Mei5 Biotech, Cat#MF681-plus-01) for 10 min. Finally, imaging was performed using a Zeiss LSM 980 confocal microscope.

qPCR. Total RNA was isolated from brown adipose tissue or brown adipocytes using TRIzol reagent (Accurate Biology, Cat#AG21101) and isopropanol (Shanghai Acmec Biochemical Technology Co., Ltd.). cDNA synthesis was performed using a cDNA synthesis kit (Abm, Cat#G490) in PCR tubes (Jet Biofil, Cat#PCR411200). Gene expression levels were quantified using a real-time PCR system (Roche) with SYBR Green (Yeasen, Cat#11201ES08). 18S mRNA was used as an internal control for data normalization. Primer sequences used for qPCR are provided in Supplementary Table 1 (Beijing Tsingke Biotech Co., Ltd.).

Transcriptome Analysis. Total RNA was extracted from BAT using the RNA Extraction Kit (Boxbio, Cat#AKNA001-1). The integrity and concentration of the RNA were assessed using iQuant Quantitation Kit (GeneCopoeia, Cat#N011-1) and the Agilent 2100 Bioanalyzer (Agilent Technologies). For RNA sequencing (RNA-Seq), 1 μg of total RNA was used to construct libraries with the NEBNext Ultra II RNA Library Prep Kit for Illumina (New England Biolabs). This process involved poly(A) selection, cDNA synthesis, adapter ligation, and amplification (YoungGen, Cat#RT101). Library concentrations were determined using a Qubit fluorometer (Thermo Fisher), and size distributions were analyzed on the Bioanalyzer. Sequencing was conducted on the Illumina NovaSeq 6000 platform, generating 150-bp paired-end reads. Raw data were processed using fastp for quality control, which included trimming adapters and filtering low-quality reads. The processed reads were then aligned to the mm10 genome using STAR. Gene expression levels were quantified using feature Counts, and differential expression analysis was performed using DESeq2. Functional enrichment analysis was conducted by Gene Denovo Biotechnology Co. (Guangzhou, China) to identify significant biological pathways and functions associated with the differentially expressed genes.

Western Blot Analysis. Brown adipose tissue or brown adipocytes were lysed with RIPA buffer (APExBIO, Cat#K1120, Houston, USA) supplemented with phosphatase and protease inhibitors (TargetMol) and sonicated using an ultrasonic processor (SCIENTZ, Cat#SCIENTZ08-IIIA). Protein concentrations were determined via BCA protein assay kit (NCM Biotech, Cat#WB6501). The protein samples were separated with ACE (Cat#ET12412) and subsequently stained using a molecular weight marker (CYTOCH, Cat#PW0011) in Tris-Glycine buffer (LABLEAD). Membranes were blocked with Fastest Blocking Reagent (HYCEZMBIO, Cat#H-YC00811) and incubated with primary antibodies: UCP1 (Diagbio, Cat#db9840) (1:1000), PRDM16 (Santa, Cat#sc-517625) (1:1000), PGC1α (SAB, Cat#37818) (1:1000), β-actin (Sino Biological, Cat#109444-T36) (1:20000), FASN (BOSTER, Cat#PB9865) (1:1000), HSL (ZENBIO, Cat#344379) (1:1000), ATGL (Abways, Cat#CY8408) (1:1000), ACC1 (HABIO, Cat#ET1609-77) (1:1000), IL6 (MULTI SCIENCES, Cat#EK2153EG) (1:1000), TNFα (AntibodySystem SAS, Cat#MHB94402) (1:1000), SOX4 (HABIO, Cat#ER1916-97) (1:1000), EBF2 (Affinity, Cat#DF13398) (1:1000), CPT1a (Biodragon, Cat#CRM8325) (1:1000), PPARα (BOSTER, Cat#A00600-2) (dilution 1:1000), ATP5a (Bioss, Cat#bsm-61444R) (dilution 1:1000), NDUFB8 (Proteintech, Cat#83216-3-RR), SDHB (CUSABIO, Cat#CSB-PA992496, https://www.cusabio.com) (dilution 1:1000), IDH (Santa, Cat#sc515396) (dilution 1:1000), CS (Proteintech, Cat#16131-1-AP) (dilution 1:1000), p-PKA (Abcam, Cat#ab75991) (dilution 1:1000), p-PKA (Abcam, Cat#ab32514) (dilution 1:1000), EMR1 (CST, Cat#70076) (dilution 1:1000), Nf-κb (CST, Cat#8242) (dilution 1:1000), Il-1β (Shanghai Hengyuan, HB1074) (dilution 1:1000), CD81 (Abcepta, Cat#ALS17719) (dilution 1:1000), TSG101 (Proteintech, Cat#14497-1-AP) (dilution 1:1000), JAK1 (Elabscience, Cat#E-AB-22202) (dilution 1:1000), JAK2 (EnoGene, Cat#E1A7126B-1) (dilution 1:1000), STAT2 (Proteintech, Cat#16674-1-AP) (dilution 1:1000), STAT3 (ELK Biotechnology, Cat#EM1207) (dilution 1:1000). After incubation with HRP-Goat Anti-Rabbit Secondary Antibody (GenScript, Cat#A00098) (dilution 1:5000) or HRP-Goat Anti-Mouse Secondary Antibody (ZUNYAN, Cat#ZYID001-0050) (dilution 1:5000), protein signals were detected using enhanced chemiluminescence (Abbkine, Cat#BMU101).

16S rRNA Sequencing Analysis. Microbial DNA was meticulously extracted from cecal fecal samples collected from mice across all experimental groups using the Fast DNA Spin Kit for Feces (MP Biomedicals, Cat#116570401). The V3−V4 region of the 16S rRNA gene was selected for amplification owing to its high variability and informativeness regarding bacterial taxonomy. PCR reactions were performed in a total volume of 25 μL, comprising 12.5 μL of 2× Phusion Master Mix (Novoprotein), 1 μL of each primer (10 μM), 1 μL of template DNA, and 10.5 μL of sterile water. The primers utilized were 341F (5′-CCTAYGGGRBGCASCAG-3′) and 806R (5′-GGACTACNNGGGTATCTAAT-3′), which are specifically designed to target the aforementioned region. The PCR products were subjected to gel electrophoresis on a 1.5% agarose gel to verify the successful amplification of the target DNA fragment and to assess the purity of the PCR product (DRAGONLAB, Cat#TC2000). Bands corresponding to the expected size of the amplified V3−V4 region were carefully excised to exclude any extraneous DNA. The DNA from the excised gel fragments was then extracted using the Qubit DNA Gel Extraction Kit (YALI Biotech, Cat#YC48001-200), following the manufacturer's protocol to ensure high-quality DNA suitable for library preparation.[28] Equal amounts of DNA from all samples were pooled, and DNA libraries were prepared using the TruSeq Nano DNA LT Sample Prep Kit (Illumina, USA). Sequencing was performed on the Illumina MiSeq PE300 platform. The sequencing data were processed using the QIIME 2 pipeline, which included denoising, filtering, and merging to generate feature tables for each group. The feature data were annotated for taxonomic classification from phylum to species levels using the Silva database. Operational taxonomic unit (OTU) abundance analysis was

https://doi.org/10.1021/acs.jafc.5c02577
J. Agric. Food Chem. 2025, 73, 21404−21421

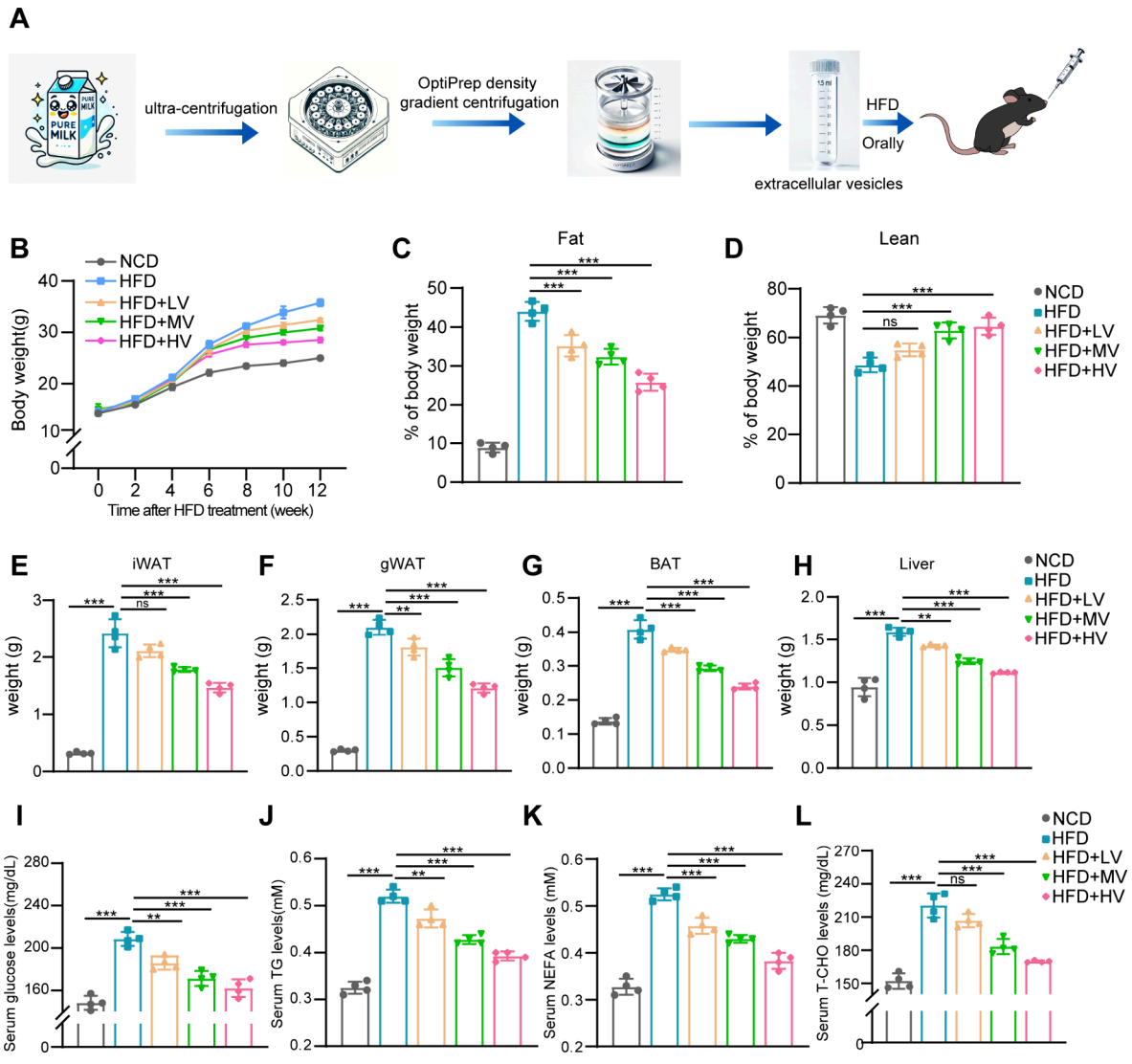

Figure 1. mEVs effectively combat obesity induced by HFD. (A) Isolation and extraction of mEVs and oral administration to mice. (B) At 6 weeks of age, mice were subjected to normal feeding (NCD), high-fat feeding (HFD), and high-fat feeding combined with the administration of vesicles (LV, MV, and HV) at different concentrations. Body weight was monitored weekly (n = 4). (C, D) At 17 weeks of age, the average lean (C) and fat (D) percentages of mice were assessed using the Echo MRI composition analyzer (n = 4). (E−H) After the feeding period, the mice were sacrificed, and the tissues of iWAT (E), gWAT (F), BAT (G), liver (H) were collected and weighed (n = 4). (I−L) At 18 weeks of age, serum glucose (I), TG (J), NEFA (K), and T-CHO (L) levels were measured in mice (n = 4). * denotes the level of statistical significance. ns, no significance, $^{**}p < 0.01$, $^{***}p < 0.001$. Data are presented as mean ± SEM. Statistical analyses were determined by one-way ANOVA followed by Tukey's test.

performed, with redundant data removed, followed by taxonomic classification from phylum to species levels. Alpha diversity, principal component analysis (PCA), and linear discriminant analysis effect size (LEfSe) were conducted using Python, the LEfSe package, and R software.

SCFA Measurement. SCFAs in fecal samples were quantified using gas chromatography-mass spectrometry (GC-MS) following a detailed sample preparation protocol. Fecal samples were first freeze-dried and ground, and 50 mg of the freeze-dried sample was placed in a 2 mL Eppendorf tube (CellProBio). To this, 500 μL of saturated sodium chloride solution was added, and the mixture was equilibrated for 30 min to ensure thorough mixing. The sample was homogenized, clumps were removed, and 20 μL of sulfuric acid was added for acidification, followed by vortexing for 30 s. Under a fume hood, 800 μL of anhydrous diethyl ether was added to extract the SCFAs, and the mixture was vortexed for an additional 30 s. The sample was then centrifuged at 14,000 rpm for 15 min to separate the phases. The upper phase was transferred to a new centrifuge tube containing (PakGent) 0.25% anhydrous.

Cell Culture and Adipocyte Differentiation. BAT stromal vascular fraction (SVF) cells were isolated from mouse brown adipose tissue following a previously described protocol.[29] The cells were cultured in growth media consisting of high-glucose DMEM (Sunncell, Cat#SA201), 100 U/ml penicillin, 100 mg/mL streptomycin (Biochannel, Cat#BCCE007), 1 mM sodium pyruvate (BasalMedia, Cat#S410JV), 1% nonessential amino acids (IMMOCELL, Cat#IMC-D07), and 10% fetal bovine serum (CellMax, Cat#SA201). To induce differentiation into mature brown adipocytes, BAT SVF cells were cultured until they reached 90−95% confluence in culture dishes (NEST, Cat#801002). Subsequently, the cells were treated for 48 h with Medium A, which contained 1 nM triiodothyronine (T3, Sigma-Aldrich, Cat#T2877), 0.125 mM indomethacin (Sigma-Aldrich, Cat#I7378), 1 μM rosiglitazone (GLPBIO, Cat#GC16444), 5 μM dexamethasone (Sigma-Aldrich, Cat#D1756), 850 nM insulin (MCE, Cat#HY-P0035), and 0.5 mM

https://doi.org/10.1021/acs.jafc.5c02577
J. Agric. Food Chem. 2025, 73, 21404−21421

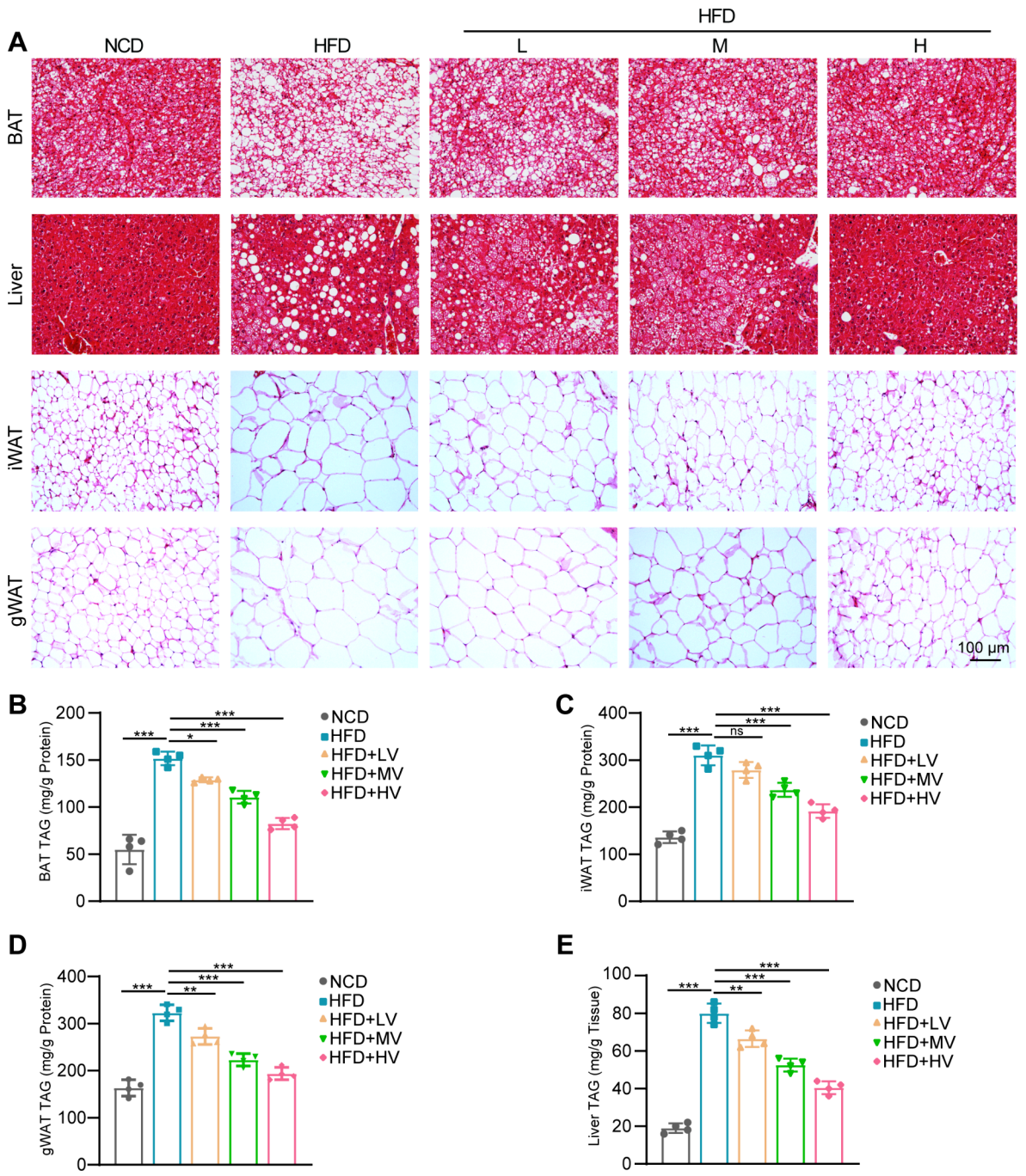

Figure 2. mEVs reduce fat accumulation in adipose tissue and the liver. (A) At 18 weeks of age, mice were sacrificed, and specific tissues, including iWAT, gWAT, BAT, and liver, were collected for H&E staining. Scale bar, 100 μm. (B–E) At 18 weeks of age, the mice from each group were sacrificed, and the TG levels in various tissues including BAT (B), iWAT (C), gWAT (D) and liver (E) were measured (n = 4). * denotes the level of statistical significance. ns, no significance, *p < 0.05, **p < 0.01, ***p < 0.001. Data are presented as mean ± SEM. Statistical analyses were determined by one-way ANOVA followed by Tukey's test.

isobutylmethylxanthine (IBMX, Sigma-Aldrich, Cat#I5879). After 48 h, the medium was replaced with Medium B, containing 1 nM T3, 1 μM rosiglitazone, and 850 nM insulin. Cells were maintained in Medium B, with medium changes every 2 days, until harvested. Both Medium A and Medium B need to be filtered before treating the cells (Schbio Biotechnology). Mature brown adipocytes were treated with vesicles at varying concentrations: 2.5 μg/mL, 5 μg/mL, and 10 μg/mL, which were designated as low, medium, and high concentrations, respectively.

Chromatin Immunoprecipitation (ChIP) Assay. Brown preadipocytes were transduced with lentiviral vectors encoding either pLV-Flag-empty or pLV-Flag-SOX4 (Shanghai Life-iLab Biotech, Cat#AC04L092). Following transduction, the cells were maintained in culture until they reached full confluence and subsequently induced to differentiate into brown adipocytes. For fixation, the cells were treated with 1% PFA at 37 °C for 15 min within a centrifuge tube (SAINING Biotechnology, Cat#3031100). Subsequently, the cells were lysed using SDS lysis buffer (Jiangsu Aidisheng Biological Technology Co., Ltd., Cat#ADS0004S0) for 15 min on ice. The total cell lysates were incubated with the indicated antibodies or FLAG Magnetic Beads (Biolinkedin, Cat#L-1011) at 4 °Cfor 8 h for DNA enrichment. The ChIP assay was executed in accordance with the

https://doi.org/10.1021/acs.jafc.5c02577
J. Agric. Food Chem. 2025, 73, 21404–21421

manufacturer's protocol. The enrichment of DNA was evaluated via qPCR and normalized to the input DNA (U&G Biotec, Cat#Q1002A). The primer sequences utilized in this experiment are detailed in Supplementary Table 1.

Oxygen Consumption Rate (OCR) Assay. Mature brown adipocytes were obtained through differentiation, and then plated onto an XFe96 cell culture microplate. The OCR was assessed utilizing the XF96 Extracellular Flux Analyzer, following the protocol provided by the manufacturer. Prior to the assay, the culture medium was exchanged with growth medium (Inner Mongolia Wanrui Biotechnology Co.,Ltd., Cat#KX-A1222), which was fortified with 25 mM glucose (AoRuiCell Bio, Cat#ORCPB0418), 1.5 mM sodium pyruvate, and 2.5 mM glutamine (Keygen BioTECH). During the OCR measurement, sequential additions of 2 μM oligomycin, 2.3 μM FCCP, and 1 μM rotenone/antimycin were employed to evaluate uncoupled respiration, maximal respiration, and nonmitochondrial respiration, respectively. The OCR measurements were normalized to the protein content of the samples.

Quantification and Statistical Analysis. Statistical analyses were performed using GraphPad Prism 8.0 software and are presented as mean ± SEM. Normality of the data was assessed using the Anderson-Darling, D'Agostino-Pearson, Shapiro-Wilk, or Kolmogorov−Smirnov tests, as appropriate. For two-group comparisons, an unpaired two-tailed Student's t test was used to assess statistical significance. For multiple group comparisons, one-way/two-way ANOVA followed by Tukey's test was applied, as indicated in the figure legends. Mouse age and sample sizes are provided in the figure legends. Significance is denoted as $^{**}p < 0.05$, $^{**}p < 0.01$, $^{***}p < 0.001$. Experimenters were not blinded to group allocation during data collection.

RESULTS

mEVs Effectively Counteract Obesity Induced by HFD. To investigate the effect of vesicles derived from different milk sources on mouse body weight, we isolated vesicles from various milk sources and administered them to mice via oral gavage while feeding them a high-fat diet (Figure S1A). As shown in Figure S1B, at week 16 of high-fat feeding, mice receiving vesicles from all three milk sources exhibited reduced body weight compared to the control group. Notably, mice receiving vesicles from camel milk displayed significantly lower body weight than those receiving vesicles from goat or cow milk. The body fat percentage results were consistent with the body weight (Figure S1C). Moreover, oral administration of camel milk vesicles significantly improved glucose tolerance and insulin sensitivity in mice, while reducing serum levels of triglycerides (TG), free fatty acids (NEFA), and total cholesterol (T-CHO) (Figure S1D-J). Based on these results, we selected camel-milk-derived vesicles (mEVs) for further investigation.

mEVs were isolated from camel milk samples through differential centrifugation and ultracentrifugation. The obtained mEVs were subsequently purified using OptiPrep density gradient centrifugation. To identify the EV-enriched fractions, Western blot analysis was performed on the fractions with increasing density, targeting the EV-specific marker protein TSG101 and CD81. As depicted in Figure S2A, the enrichment of TSG101 and CD81 in fractions 3 to 5, which correspond to a density range of 1.4−1.8 g/mL, is consistent with the buoyant density of mEVs reported in previous studies.[30,31] Fraction 5, enriched in TSG101 and CD81, was selected for further analysis. Additionally, transmission electron microscopy (TEM) revealed the presence of vesicular structures in the samples (Figure S2B), and nanoparticle tracking analysis (NTA) showed a major peak at 132.6 nm for mEVs (Figure S2C,D). These results demonstrate that mEVs were successfully isolated and characterized from camel milk.

To assess the impact of mEVs on body weight and serum lipids, we orally administered mEVs with low, medium, and high concentrations to mice while feeding them a high-fat diet (HFD) for subsequent functional analysis (Figure 1A). As the concentration of the vesicles increased, the rate of body weight gain in mice slowed compared to those in the HFD group (Figure 1B). By week 12, the body weight of the HFD group was 35.77 ± 0.38 g, while the body weights of the groups receiving low-dose, medium-dose, and high-dose vesicles alongside HFD were 31.72 ± 0.29 g, 31.03 ± 0.33 g, and 28.50 ± 0.31 g, respectively (Figure 1B). According to body composition analysis, mEVs feeding decreased body fat but increased body lean composition (Figure 1C,D). After sacrificing the mice, the iWAT, gWAT, BAT, and liver were collected and weighed. The weight of the iWAT, gWAT, BAT, and liver of the MV and HV group was significantly lower than the HFD group, whereas there was no significant difference in iWAT between the LV group and the HFD group (Figure 1E−H). To further investigate the effects of mEVs on serum glucose and serum lipid levels in mice, we measured serum glucose, TG, NEFA, and T-CHO. Serum glucose, TG, NEFA, and T-CHO were significantly lower in MV and HV group compared to the HFD group (Figure 1I−L). However, the LV group did not exhibit a significant reduction in serum T-CHO (Figure 1L). To further examine the impact of mEVs on liver function, we measured serum AST, ALT, and LDL levels. Serum AST, ALT, and LDL levels were highest in the HFD group (Figure S3A−C). As the mEVs concentration increased, the levels of these markers gradually decreased in the MV and HV groups, suggesting an improvement in liver function (Figure S3A−C). These results suggest that oral administration of mEVs reduces body weight gain, fat mass, and improve metabolic and liver function in high-fat-diet-fed mice, effectively preventing diet-induced obesity and dyslipidemia.

mEVs Reduce Lipid Accumulation in Adipose Tissue and Liver. To further confirm the effect of mEVs on lipid accumulation in adipose tissues and liver, we performed H&E staining experiments. As shown in Figure 2A, compared to the NCD group, high-fat feeding significantly promoted lipid accumulation in the BAT, iWAT, gWAT, and liver. With increasing mEVs concentrations, the lipid accumulation in these tissues gradually decreased (Figure 2A). However, the lipid accumulation levels in HV group did not return to the levels seen in the NCD group (Figure 2A). To further validate the H&E staining results, we measured the TG levels in WAT and liver. As shown in Figure 2B−E, compared to the HFD group, mice in the MV and HV groups exhibited a significant reduction in TG accumulation in three adipose tissues and liver ($p < 0.001$). However, in LV group, although there was a trend toward decreased TG levels in iWAT, no significant difference was observed compared to the HFD group ($p > 0.05$) (Figure 2C). Overall, these results demonstrate that mEVs reduced lipid and TG accumulation in adipose tissues and liver in high-fat-diet-fed mice, with more pronounced effects at higher doses.

mEVs Significantly Facilitate Thermogenesis of Mice. Previous studies have demonstrated that an enhanced thermogenic function of BAT can increase energy expenditure and counteract weight gain.[32] To verify whether mEVs enhance the thermogenic capacity of BAT, we measured the core body temperature of mice in each group under room

https://doi.org/10.1021/acs.jafc.5c02577
J. Agric. Food Chem. 2025, 73, 21404−21421

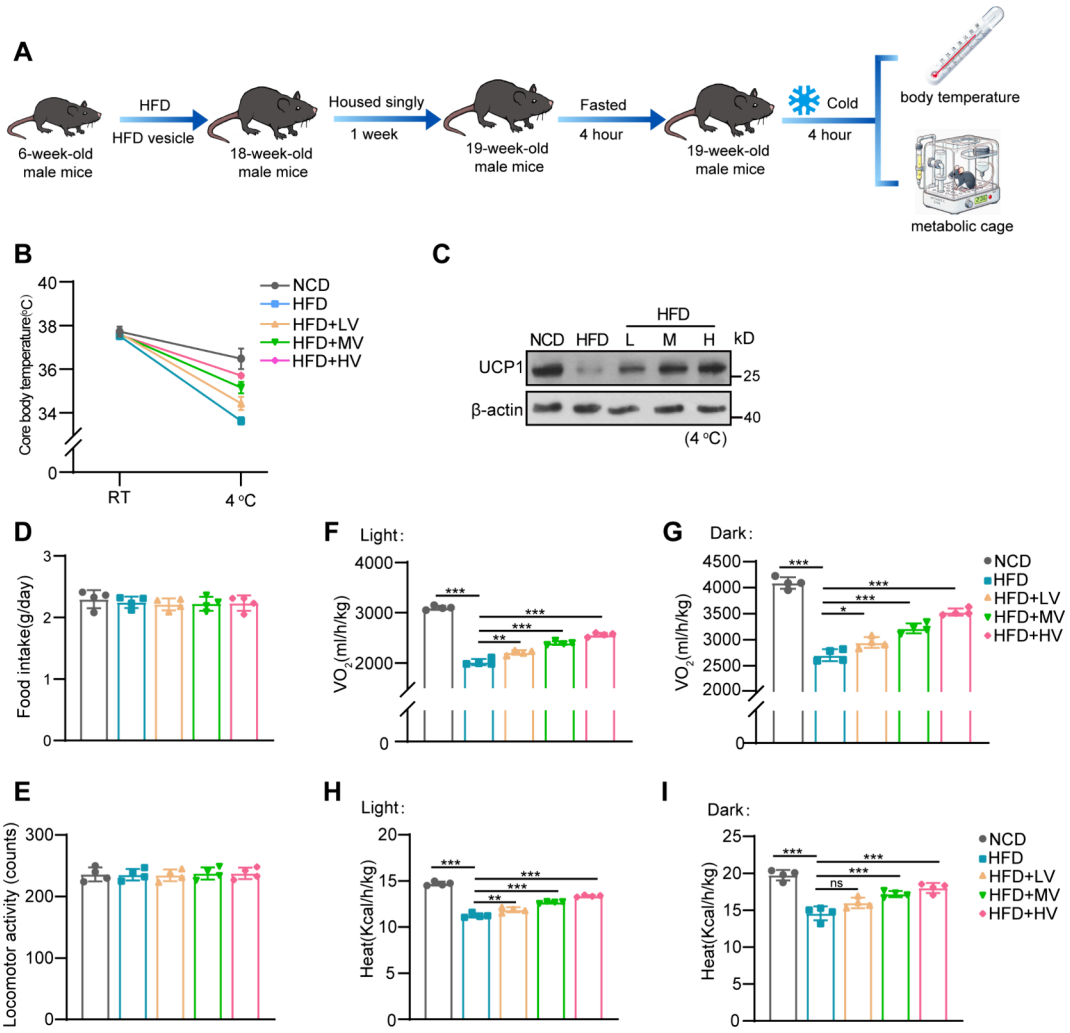

Figure 3. mEVs significantly enhance thermogenesis in mice. (A) This schematic illustrates the construction of the mouse model. At the end of the experiment, the 19-week-old mice were used for metabolic cage analysis and body temperature measurement. (B) The variations in core body temperature were observed in mice from different groups. Additionally, changes were measured during acute cold exposure at 4 °C for 4 h (n = 4). (C) The protein levels of UCP1 in the BAT of mice. (D−I) At 18 weeks of age, the mice were individually housed for 1 week before being used in the metabolic cage experiment. Food intake and activity are shown in (D) and (E). Oxygen consumption (F, G) and heat production (H, I) of the mice during both day and night were measured (19-week-old, n = 4). * denotes the level of statistical significance. ns, no significance, *p < 0.05, **p < 0.01, ***p < 0.001. Data are presented as mean ± SEM. Statistical analyses were determined by one-way ANOVA followed by Tukey's test.

temperature (RT) or acute cold exposure at 4 °C for 4 h (Figure 3A). As shown in Figure 3B, all groups had comparable core temperatures of 38 °C when kept at room temperature. However, following 4 h of cold exposure at 4 °C, mice in the oral mEVs group effectively mitigated the decrease in body temperature compared to the HFD group (Figure 3B). Consistently, UCP1 expression was significantly increased in BAT at 4 °C with the elevated concentration of orally administered mEVs compared to the HFD group (Figure 3C). To further confirm the effects of mEVs on the systemic metabolism of mice, we assessed the oxygen consumption and heat production of all groups of mice using a metabolic cage system. As shown in Figure 3D,E, feeding with mEVs did not affect the food intake and activity of mice. However, the oral administration of mEVs significantly increased the oxygen consumption and heat production of the mice, both during the day and at night, compared to the HFD group (Figure 3F−I). Interestingly, the mice in LV group showed no difference in heat production during the night compared to the HFD group (Figure 3I). Collectively, these findings suggested that mEVs significantly enhanced thermogenesis and energy expenditure in mice.

mEVs of High Concentration Promote the Expression of Thermogenic Genes and Suppress the Expression of Lipid Synthesis and Inflammation-Related Genes. Given the enhanced ability of mEV-fed mice to maintain body temperature under acute cold stimulation, we focused on the impact of mEVs on BAT. To gain further insight into the effect of mEVs on BAT function, we conducted RNA sequencing on BAT tissues from mice of HFD groups and HV groups. A significant distance was observed between the HFD and HV groups, highlighting the considerable differences in gene expression levels between the HFD and HV groups (Figure 4A). As illustrated in Figure 4B, the HV group exhibits 3028 upregulated genes and 1353 downregulated genes relative to the HFD group. Among the downregulated genes, several are involved in lipid synthesis, such as *Fasn*, *Fads3*, and *Acly*, as well as inflammatory genes like *Il6*, *Ccl6*, and *Il10ra* (Figure 4C). The upregulated genes include thermogenesis-related genes, such as *Ucp1* and *Prdm16*, along with genes associated

https://doi.org/10.1021/acs.jafc.5c02577
J. Agric. Food Chem. 2025, 73, 21404−21421

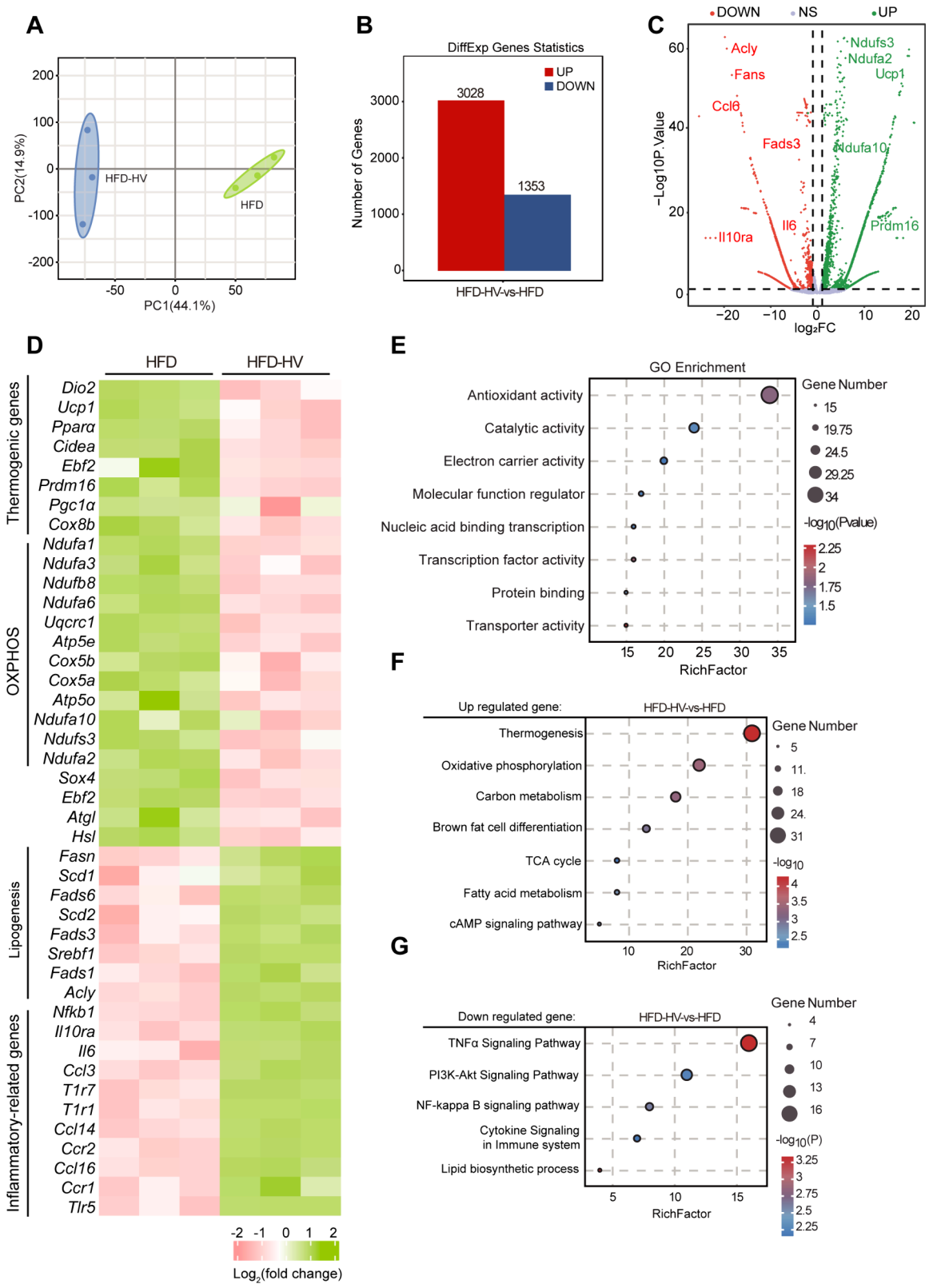

Figure 4. mEVs of high concentration promote thermogenic gene expression and inhibit lipid synthesis and inflammation-related genes. (A) PCA analysis of the two groups of 18-week-old mice. (B) The number of upregulated and downregulated genes in the two groups of mice. (C, D) Volcano plot (C) and heatmap (D) analysis of the BAT tissue of the two groups of mice. (E) KEGG pathway analysis of the BAT in the two groups. (F, G) GO analysis of the upregulated and downregulated genes in the BAT of the two groups.

with oxidative phosphorylation, including *Ndufs3* and *Ndufa2* (Figure 4C). To validate these gene alterations, we reanalyzed the RNA-Seq data and performed heatmap analysis. Figure 4D demonstrates that the upregulated genes are primarily involved in thermogenesis (including *Ucp1*, *Dio2*, *Ppara*, *Ebf2*, and *Prdm16*) and oxidative phosphorylation (including *Ndufa1*,

https://doi.org/10.1021/acs.jafc.5c02577
J. Agric. Food Chem. 2025, 73, 21404−21421

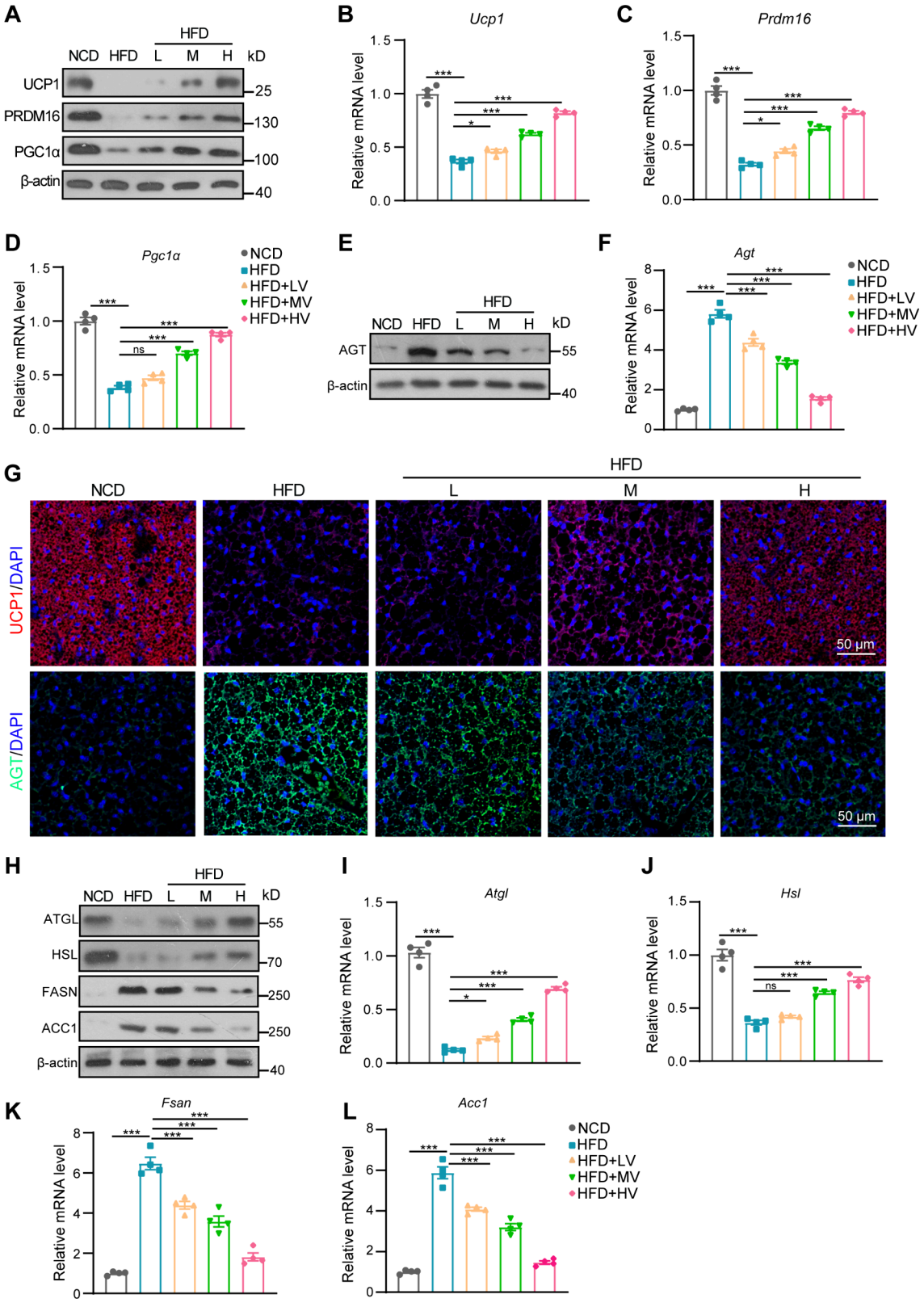

Figure 5. mEVs stimulate thermogenic gene expression and suppress inflammation and lipid synthesis genes. (A) The protein levels of UCP1, PRDM16, and PGC1α in the BAT of 18-week-old mice. (B–D) The mRNA levels of *Ucp1* (B), *Prdm16* (C), and *Pgc1α* (D) in the BAT of mice from each group (18-week-old, $n = 4$). (E) The protein levels of AGT in the BAT of mice from each group. (F) The mRNA levels of *Agt* in the BAT of mice from each group (18-week-old, $n = 4$). (G) Immunostaining images of UCP1 and AGT in the BAT of mice from each group. Scale bar, 50 μm. (H) The protein levels of HSL, ATGL, FASN, and ACC1 in the BAT of mice from each group. (I–L) The mRNA levels of *Hsl* (I), *Atgl* (J), *Fasn* (K), and *Acc1* (L) in the BAT of mice from each group (18-week-old, $n = 4$). * denotes the level of statistical significance. ns, no significance, $*p < 0.05$, $***p < 0.001$. Data are presented as mean ± SEM. Statistical analyses were determined by one-way ANOVA followed by Tukey's test.

https://doi.org/10.1021/acs.jafc.5c02577
J. Agric. Food Chem. 2025, 73, 21404–21421

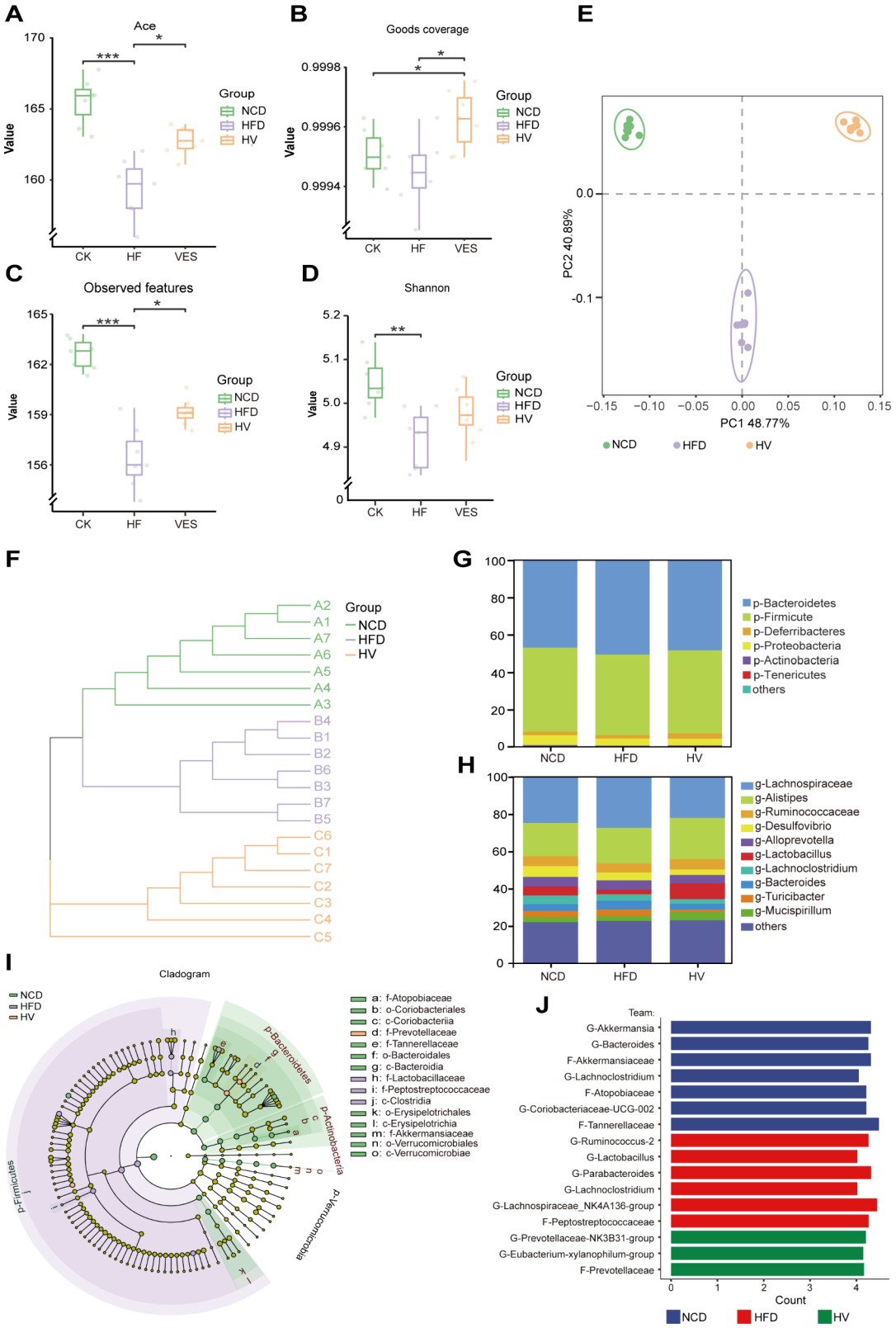

Figure 6. mEVs induce alterations in gut microbiota and metabolic reprogramming in high-fat-diet mice. (A–D) Assessment of α-diversity in the gut microbiota across different groups of mice (18-week-old), using four indices: ACE (A), Good's coverage (B), observed features (C), and Shannon (D) index. (E) β-diversity analysis of gut microbiota composition using nonmetric multidimensional scaling (NMDS) based on Bray–Curtis dissimilarities. (F) Phylogenetic evolutionary tree analysis of gut microbiota structure, highlighting the differences in microbial community composition across experimental groups. (G) Phylum and genus level composition and abundance of gut microbiota in different experimental groups, with focus on key phyla and their role in gut homeostasis. (H, I) LEfSe discriminant analysis of gut microbiota taxa (filter test using Kruskal–Wallis, Wilcoxon, LDA > 3). * denotes the level of statistical significance. *$p < 0.05$, **$p < 0.01$, ***$p < 0.001$. Data are presented as mean ± SEM. Statistical analyses were determined by one-way ANOVA followed by Tukey's test.

https://doi.org/10.1021/acs.jafc.5c02577
J. Agric. Food Chem. 2025, 73, 21404–21421

Ndufb8, and *Cox5b*), while the downregulated genes are linked to lipid synthesis (including *Fasn*, *Fads6*, *Scd1*, and *Acly*) and inflammation-related pathways (including *Nfkb1*, *Il6*, *Ccr1*, and *Tlr5*). Gene Ontology analysis of the upregulated genes revealed their enrichment in antioxidant activity, catalytic activity, and the electron carrier activity (Figure 4E). Functional enrichment analysis of the upregulated genes revealed significant enrichment in pathways related to thermogenesis, oxidative phosphorylation, fatty acid oxidation, branched-chain amino acid catabolism (Figure 4F). The downregulated genes were primarily enriched in the TNFα signaling pathway, NF-kappa B signaling pathway, and lipid biosynthetic process (Figure 4G). These findings indicate that mEVs promoted the expression of thermogenic genes in BAT and suppressed the expression of lipid synthesis genes.

mEVs Promote the Expression of Thermogenic Genes and Suppress the Expression of Inflammation and Lipid Synthesis Genes. To further validate the RNA-seq results, we conducted experimental verification by collecting BAT tissues from the NCD, HFD, LV, MV, and HV groups for Western blot, immunofluorescence, and qPCR experiments. As shown in Figure 5A, the protein expression levels of UCP1, PGC1α, and PRDM16 in the BAT tissue of HFD mice were significantly lower than those in NCD mice. With increasing mEVs concentration, the protein expression levels of UCP1, PGC1α, and PRDM16 gradually increased relative to the HFD group. The qPCR results further confirmed the Western blot findings (Figure 5B−D). Angiotensinogen (AGT) is a protein marker used to assess the "whitening" of BAT. Increased AGT expression in BAT indicates a shift toward a white-fat-like phenotype, often linked to reduced thermogenic function and impaired brown adipocyte identity.[33] High-fat feeding significantly promotes the expression levels of AGT, while mEVs feeding markedly inhibits the upregulation of AGT (Figure 5E,F). Immunofluorescence results further confirmed the changes in the expression levels of UCP1 and AGT proteins (Figure 5G). Furthermore, we identified key proteins within various signaling pathways that were highlighted through RNA-Seq Initially, we focused on the oxidative phosphorylation pathway, and found that the protein levels of MTCOI, NDUFB8, ATP5a, and SDHB significantly increased with the elevated concentration of orally administered mEVs compared to the HFD group (Figure S4A). Additionally, we investigated other pathways, including the carbon metabolism pathway, the TCA cycle, and the cAMP pathway. The expression levels of key proteins in these pathways, such as CPT1A, PPARα, IDH1, and PKA, were found to be consistent with those observed in the oxidative phosphorylation pathway (Figure S4B−E). Finally, we explored the TNF-α, NF-κB, and Cytokine Signaling in Immune System pathways. Notably, the expression levels of key proteins in these pathways, including TNF-α, IL-6, IL-1β, NF-κB, EMR1, JAK1, and STAT2, exhibited an opposite trend compared to those in the oxidative phosphorylation pathway (Figure S4F−H). These results further substantiate the findings from the RNA-Seq analysis.

PKA activation of hormone-sensitive lipase (HSL) and adipose triglyceride lipase (ATGL) enhances triglyceride lipolysis, leading to an increased release of FFAs for mitochondrial utilization, thereby promoting thermogenesis in BAT.[34,35] To investigate the effect of mEVs on lipolysis in BAT, we assessed the expression of HSL and ATGL at both protein and mRNA levels. As shown in Figure 5H−J, the expression levels of HSL and ATGL were significantly higher in the MV and HV groups compared to the HFD group. However, oral administration of low-concentration mEVs did not promote HSL expression ($p > 0.05$) (Figure 5J). Previous research has indicated that the "whitening" of BAT is associated with the promotion of lipogenesis and inflammation within BAT.[36] Therefore, we further evaluated the expression of lipogenesis genes, ACC and FASN, in the BAT of mice from each group. As depicted in Figure 5H,K,L, the HFD group showed a significant upregulation of both ACC and FASN in the BAT compared to the NCD group. Notably, with increasing mEVs concentration, the expression levels of ACC and FASN gradually decreased (Figure 5K,L). Collectively, mEVs promote thermogenesis, enhance lipolysis, and suppress lipogenesis and inflammation in BAT.

mEVs Enhance Thermogenic Gene Expression and Oxygen Consumption Rates *In Vitro*. To further examine the role of mEVs in thermogenic gene regulation within BAT, stromal vascular fractions (SVFs) were isolated from BAT and induced to differentiate into brown adipocytes. The cells were treated with varying concentrations of mEVs and subsequently harvested for qPCR analysis, Western blotting analysis, and OCR assays (Figure S5A). As demonstrated in Figure S5B, the TG content decreased progressively with increasing concentrations of mEVs compared with the control cells. Moreover, mEV treatment significantly upregulated the expression of UCP1 and PRDM16 compared to the control group, while leading to a progressive downregulation of AGT expression with increasing concentrations (Figure S5C−F). In line with the observed increase in thermogenic gene expression, mEVs treatment also significantly enhanced both the basal and maximal respiratory rates of the cells (Figure S5G−I). Collectively, these findings indicate that mEVs promote thermogenic gene expression and increase oxygen consumption rate in *vitro*.

Gut Microbiota Alterations and Metabolic Reprogramming Induced by mEVs in High-Fat-Diet Mice. To investigate the impact of vesicles on microbial dysbiosis induced by high-fat diet, we performed 16S rRNA sequencing of the gut microbiota from cecal fecal samples in different experimental groups. Microbial community richness, evenness, and diversity were assessed from four perspectives using the ACE index, Good's coverage index, Observed features, and Shannon index. Despite variations in the numerical range of these four indices, they displayed similar trends. The results indicated that, compared to the NCD group, α-diversity of the gut microbiota was reduced under HFD conditions, whereas mEVs intervention had a partial ameliorating effect on the decreased diversity (Figure 6A−D). Further, β-diversity was statistically analyzed using nonmetric multidimensional scaling (NMDS) based on Bray−Curtis dissimilarities. In Figure 6E, the three groups are clearly separated, with two principal components explaining 88% of the variation, suggesting significant group differences. Additionally, samples within the same group were closely clustered, indicating successful sampling. Moreover, an evolutionary tree constructed for the samples visually demonstrated changes in gut microbiota structure, with closer phylogenetic relationships and tighter groupings observed in the same group, suggesting higher diversity and stability within groups (Figure 6F). Phylum-level analysis identified *Bacteroidetes*, *Firmicutes*, *Deferribacteres*, *Proteobacteria*, and *Actinobacteria* as dominant phyla, with varying abundances across groups. At the phylum level, mEVs

https://doi.org/10.1021/acs.jafc.5c02577
J. Agric. Food Chem. 2025, 73, 21404−21421

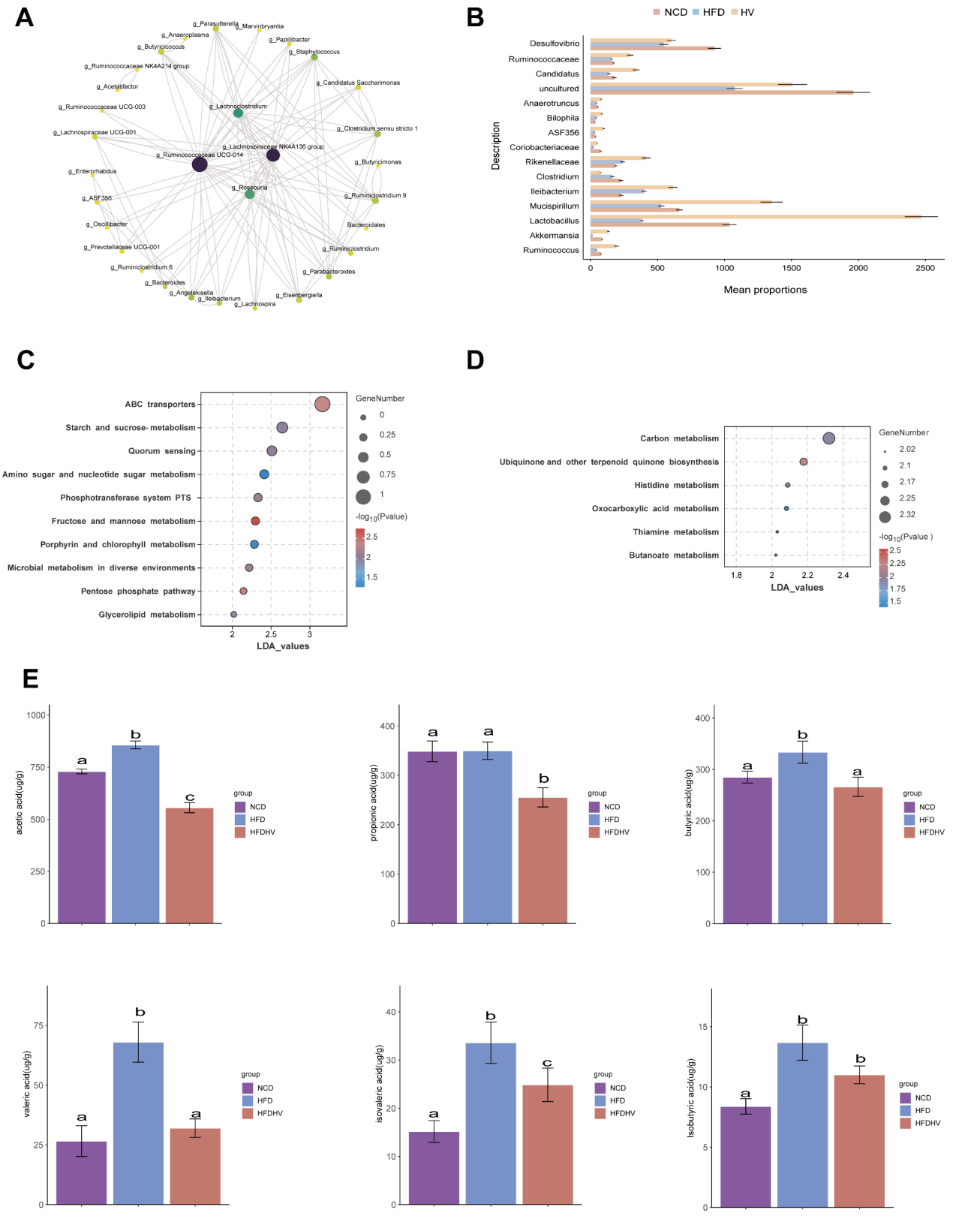

Figure 7. mEVs restore gut homeostasis and regulate SCFA production. (A) Pearson correlation network of genus-level microbial abundance, excluding self-correlation, showing interaction mechanisms and regulatory relationships among microbial genera. (B) Top 16 genera with significant differences in abundance across experimental groups, highlighting the impact of milk vesicles on *Lactobacillus* and *Akkermansia* recovery. (C) KEGG functional enrichment analysis of gut microbiota in the NCD group, showing enriched metabolic pathways involved in basic metabolism and material transport. (D) KEGG functional enrichment analysis of gut microbiota in the HV group, indicating significant changes in carbon metabolism, thiamine metabolism, and butanoate metabolism pathways. (E) SCFA concentration changes across experimental groups, demonstrating increased SCFA levels in the HFD group and the potential restorative effect of milk vesicles on SCFA levels in the HV group.

https://doi.org/10.1021/acs.jafc.5c02577
J. Agric. Food Chem. 2025, 73, 21404−21421

Figure 7. continued

Components with no identical letters indicate no significant difference ($p < 0.05$). Data are presented as mean ± SEM. Statistical analyses were determined by one-way ANOVA followed by Tukey's test.

intervention reversed the high-fat-diet-induced shift in microbial composition, significantly reducing the *Firmicutes*/*Bacteroidetes* ratio and suppressing *Proteobacteria* abundance (Figure 6G). Simultaneously, genus-level analysis demonstrated that mEVs significantly modulated gut microbiota composition, including increasing beneficial genera such as *Alloprevotella* and *Lactobacillus*, while reducing taxa associated with dysbiosis like *Desulfovibrio* (Figure 6H). Analysis of the top 10 genera revealed that, compared to the NCD group, the HFD group exhibited an increased abundance of *Lachnospiraceae* and *Alistipes*, while the abundance of *Lactobacillus* was reduced (Figure 6H). However, the mEVs intervention was able to reverse this trend, enhancing the abundance of beneficial taxa and restoring gut homeostasis (Figure 6I). Considering the significant impact of mEVs on fatty acid metabolism, this study investigated the alterations in dominant gut microbial communities. In the NCD group, seven predominant microbial communities were identified, including *Akkermansia*, *Akkermansiaceae*, and *Atopobiaceae* (Figure 6J). In contrast, the HV group displayed a reduced diversity of dominant microbial communities, with only three core taxa, including *Prevotellaceae-NK3B31* group. By comparison, the HFD group exhibited six core genera, such as *Lactobacillaceae*, *Parabacteroides*, and *Lactobacillus* (Figure 6J). These shifts in the composition and abundance of core microbial communities may play a pivotal role in modulating host metabolic processes.

mEVs Restore Gut Homeostasis and Regulate SCFA Production. The genus-level microbial abundance data were further analyzed using pearson correlation to explore interaction mechanisms and regulatory relationships, with a focus on identified species while excluding self-correlation. The network diagram visualizes these interactions, where each node represents a microbial genus, and the size of the node corresponds to the relative abundance of that genus within the microbial community. The connecting lines between nodes indicate significant correlations, with the thickness of the lines reflecting the strength of the correlation. A thicker line signifies a stronger correlation between the connected genera (Figure 7A). Notably, the *Lachnospiraceae NK4A136* group exhibited the most extensive connections with other genera within the network. Similarly, genera such as *Ruminococcaceae UCG-014*, *Roseburia*, and *Lachnoclostridium* were also found to be highly interconnected, underscoring their potential importance in shaping microbial community structure and function. Furthermore, as shown in Figure 7B, the top 15 genera with the most significant differences are highlighted. Notably, *Desulfovibrio* and *Mucispirillum* maintained relatively high abundance across all treatments, while mEVs had a positive effect on the recovery of *Lactobacillus* and *Akkermansia*, a finding that was further supported by LDA (Figure 7B). To explore the potential functional roles of the gut microbiota in metabolic processes, we conducted KEGG functional enrichment analysis on the microbial communities of each group. This analysis involved mapping the identified microbial taxa to specific KEGG Orthology (KO) terms and pathways, which allowed to predict the metabolic capabilities and functional profiles of the gut microbiota. By comparing the relative abundance of these KO terms across different groups, we aimed to identify significant differences in metabolic functions that could be associated with the intervention of mEVs. In the NCD group, enriched functions of the gut microbiota were primarily focused on basic metabolic pathways, such as starchand sucrose metabolism, fructoseand mannose metabolism, and porphyrin and chlorophyll metabolism. These pathways contribute to maintaining normal metabolic balance and energy supply in the gut. Additionally, the NCD group's microbiota exhibited heightened functions related to material transport, including ABC transporters and microbial metabolism in diverse environments. These findings likely reflect the adaptive capacity of the gut microbiota to its environment and its role in facilitating material transport (Figure 7C). In the HV group, functional enrichment analysis revealed significant changes in the metabolic functions of the gut microbiota. Compared to the HFD group, the HV group exhibited increased activity in carbon metabolism and thiamine metabolism pathways (Figure 7D). Additionally, the Butanoate metabolism pathway was enriched in the HV group, indicating that mEVs have a regulatory effect on the gut microbiota's metabolic pathways, particularly in SCFA metabolism (Figure 7D).

SCFAs, including acetate, propionate, and butyrate, are major products of microbial fermentation of dietary fibers and other indigestible carbohydrates in the gut. They play crucial roles in host health, providing energy and regulating glucose and lipid metabolism. The balance of SCFA concentrations is vital for gut health, as both elevated and reduced levels of SCFAs may lead to adverse physiological responses. In this study, compared to the NCD group, the HFD group exhibited a significant increase in SCFA levels (Figure 7E). However, the high-concentration mEVs partially restored the levels of SCFAs (Figure 7E). Notably, elevated SCFAs in the HFD group were associated with specific alterations in gut microbiota composition, characterized by a significant increase in the abundance of mucin-degrading bacteria such as *Mucispirillum* and the inhibition of butyrate metabolism pathway expression. In contrast, the partial restoration of SCFAs in the HV intervention group was associated with the recovery of protective bacterial taxa and significant enrichment of the butyrate metabolism pathway (Figure 7B,D,E). This finding suggests that mEVs may restore gut homeostasis by modulating microbial metabolic pathways, thereby exerting a positive regulatory effect on gut dysfunction induced by a high-fat diet.

mEVs Promote the Expression of Thermogenic Genes through SOX4-EBF2 in BAT. To further investigate the mechanism by which mEVs promote the expression of thermogenic genes in BAT and mitigate obesity, we analyzed RNA-seq data. As shown in Figure 4D, the expression of SOX4 and EBF2 in the BAT of the HV group was significantly higher compared to the HFD group. Previous studies have indicated that SOX4 or EBF2 can promote the expression of thermogenic genes in BAT.[9] And the mice overexpressing SOX4 or EBF2 exhibit higher heat production and are more resistant to obesity and related metabolic disorders.[9,11,37] Additionally, intensive studies have elucidated that both obese animals and humans exhibit impaired thermogenic capacity in

https://doi.org/10.1021/acs.jafc.5c02577
J. Agric. Food Chem. 2025, 73, 21404−21421

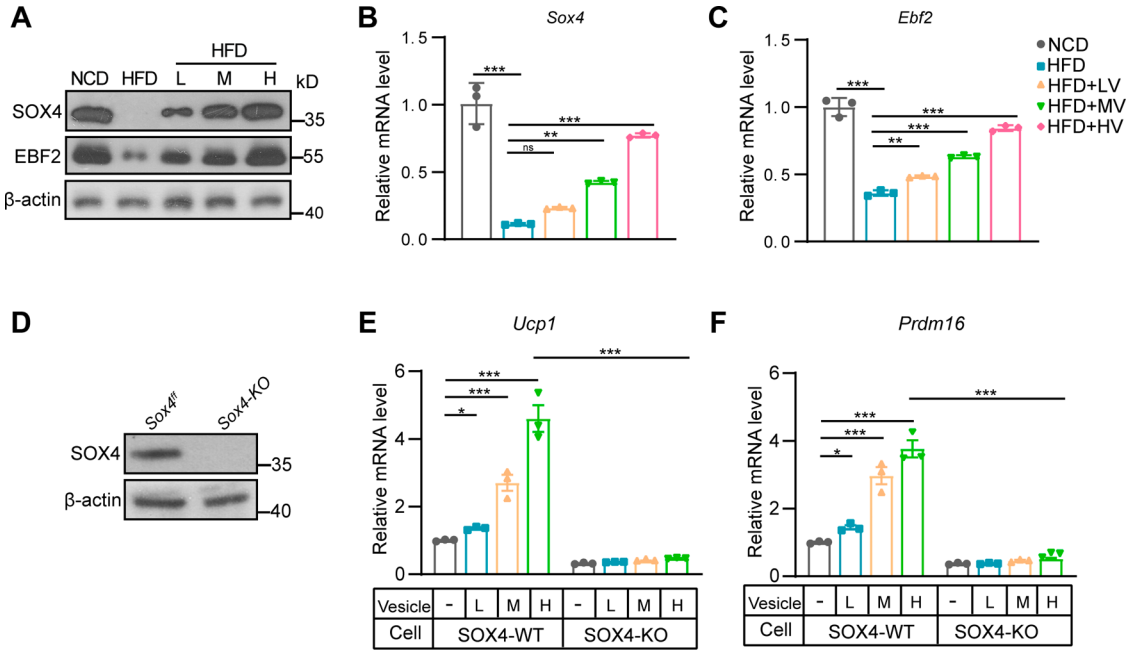

Figure 8. mEVs enhance the expression of thermogenic genes in BAT via the SOX4-EBF2 pathway. (A−C) The expression of SOX4 and EBF2 proteins and mRNA in BAT from different groups (18-week-old mice, $n = 4$). (D) The protein levels of SOX4 in both groups of cells. (E, F) The mRNA levels of *Ucp1* and *Prdm16* in the BAT stromal vascular fraction (SVF) from *SOX4*^{ff} and *SOX4-KO* mice with vesicle treatment. * denotes the level of statistical significance. *$p < 0.05$, **$p < 0.01$, ***$p < 0.001$. Statistical analyses were determined by one-way ANOVA (B, C) or two-way ANOVA (E, F) followed by Tukey's test.

BAT.[38] Given this, we first compared RNA-seq data from HFD-HV BAT (Up-HFD-HV vs HFD) with data from HFD BAT (Down-HFD vs NCD; GSE116225). Among these genes, 1,653 genes were found to overlap, including Sox4, Ebf2, Ucp1, and Pgc1α (Figure S6A). Interestingly, we also observed that, similar to the phenotypes of mice overexpressing SOX4 or EBF2, oral administration of mEVs resulted in increased expression of thermogenic genes in BAT and counteracted high-fat-diet-induced weight gain.[37,39,40] We speculate that mEVs may regulate BAT thermogenesis through the SOX4-EBF2 pathway. To further validate our hypothesis, we reanalyzed RNA-seq data from HFD-HV BAT alongside data from *Sox4-MKO* (GSE263445) and *Ebf2-AKO* (GSE144188) BAT. As shown in the Figure S6B, among the up-regulated genes in HFD-HV BAT, 235 genes overlapped with those down-regulated upon knockout of SOX4 and EBF2. These overlapping genes were primarily enriched in pathways related to thermogenesis, oxidative phosphorylation, and the TCA cycle (Figure S6B). Based on this, we examined the protein and mRNA levels of SOX4 and EBF2 in the BAT of different groups. In the HFD group, the expression of SOX4 and EBF2 in BAT was significantly lower than in the control group, and the concentration of mEVs was positively correlated with the expression levels of both SOX4 and EBF2 (Figure 8A−C). Furthermore, we identified putative SOX4 binding sites (AACAAAG) in the EBF2 promoter region, and the binding of SOX4 to the EBF2 promoter increased with higher concentrations of mEVs (Figure S6C,D). To confirm whether the mEVs-induced promotion of thermogenic genes in BAT is dependent on SOX4, we isolated the BAT stromal vascular fraction cells (SVFs) from both *Sox4*^{ff} and *SOX4-KO* mice and stimulated them with varying concentrations of mEVs (Figure 8D). As shown in Figure 8E,F, increasing mEVs concentrations effectively enhanced the expression of thermogenic genes, whereas the absence of SOX4 inhibited the mEVs-mediated promotion of thermogenic gene expression. These findings suggest that mEVs promote the expression of thermogenic genes through the SOX4-EBF2 pathway.

DISCUSSION

Enhancing the thermogenic activity of BAT augments energy expenditure, mitigates adiposity, and restores metabolic homeostasis, positioning BAT activation as a promising therapeutic approach for obesity and associated metabolic disorders.[41] Milk-derived extracellular vesicles, which are equipped with a bilayer lipid structure that protects their luminal cargo such as proteins and RNA, play significant roles in disease progression and human health.[31] However, the roles and underlying mechanisms of milk-derived extracellular vesicles in regulating whole-body energy homeostasis and combating obesity remain poorly understood. Here, we found that the mice receiving vesicles from camel milk exhibited significantly lower body weight and fat percentage compared to those receiving vesicles from goat or cow milk. Additionally, we found that oral administration of mEVs effectively mitigated obesity, significantly reducing body fat percentage, serum TG, serum NEFA, and T-CHO levels in *vivo*. Notably, mEVs enhanced the thermogenic function of BAT, as evidenced by a smaller decrease in core body temperature during cold exposure compared to the HFD group. Moreover, mEVs increased oxygen consumption and heat production, indicating enhanced energy expenditure.[42] RNA sequencing of BAT tissues revealed upregulation of thermogenesis-related genes such as Ucp1 and Prdm16, as well as genes involved in oxidative phosphorylation, suggesting that mEVs promote thermogenic capacity. Additionally, mEVs suppressed the expression of lipid synthesis genes and inflammatory markers, highlighting their potential to modulate metabolic processes.

https://doi.org/10.1021/acs.jafc.5c02577
J. Agric. Food Chem. 2025, 73, 21404−21421

These findings underscore the dual benefits of mEVs in alleviating obesity and enhancing metabolic homeostasis by improving energy balance and thermogenesis in *vivo*. These metabolic benefits may stem from the combined effects of various bioactive molecules in camel-milk-derived EVs, such as miRNAs, proteins, and active lipids. Studies suggest that regulatory miRNAs in EVs, such as miR-148a and the let-7 family, may cross the intestinal barrier and target epigenetic regulators. Furthermore, the bioactive lipids in EVs may contribute to reshaping the gut microbiota, thereby promoting butyrate metabolism.[43] It is known that butyrate can enhance mitochondrial biogenesis through PGC-1α, a mechanism consistent with the transcriptomic data from BAT.[22,44] Furthermore, mEVs significantly enhanced the expression of thermogenic genes in brown adipocytes and increased the OCR in *vitro*. Thus, mEVs emerge as a promising noninvasive therapeutic strategy for obesity and related metabolic disorders, positioning them as a novel platform for future biomedical applications.

BAT plays a crucial role in maintaining body temperature via nonshivering thermogenesis and in regulating energy homeostasis by combating obesity.[10] These functions are mediated by the consumption of triglycerides to produce heat and counteract energy surplus. When the function of BAT is disrupted, it results in the whitening of BAT, and mice exhibit hypothermia upon acute cold exposure, along with obesity induced by a high-fat diet.[5] Consequently, the functional evaluation of BAT is currently primarily assessed through acute cold exposure and HFD challenges. Feeding with an HFD provides a more comprehensive assessment of BAT function, including thermogenesis, inflammation, fibrosis, lipolysis, and lipogenesis.[45] Based on the RNA-Seq results, we observed a significant increase in the expression of SOX4 and EBF2 in the BAT of mice treated with mEVs. Previous studies have shown that SOX4 and EBF2 can regulate the transcription of thermogenic genes such as Ucp1 and Pgc1α.[39] Interestingly, similar to the phenotypes of mice overexpressing SOX4 or EBF2, oral administration of mEVs increased the expression of thermogenic genes in BAT and counteracted high-fat-diet-induced weight gain.[9,37] Further analysis revealed that mEVs, in conjunction with SOX4 and EBF2, collaboratively regulate pathways related to thermogenesis, oxidative phosphorylation, and the TCA cycle. Consequently, SOX4 enhances BAT thermogenic function through the SOX4-EBF2 pathway. Moreover, the loss of SOX4 significantly inhibited the mEV-induced activation of thermogenic genes. However, a limitation of our study is the lack of in vivo functional validation using brown adipose tissue-specific Sox4 knockout mice. Future studies should focus on further elucidating the in vivo mechanisms by which mEVs regulate thermogenic genes. Additionally, while the potential involvement of the SOX4-EBF2 pathway has been highlighted, other mechanisms of mEV action remain unexplored and require further investigation to fully elucidate the specific signaling pathways involved.

mEVs play a pivotal role in modulating gut microbiota and enhancing metabolic functions. They promote the proliferation of beneficial bacteria, such as *Lactobacillus* and *Akkermansia*, while inhibiting the growth of harmful microbes, thereby strengthening gut barrier integrity and reducing intestinal permeability. This modulation leads to improved immune function and the maintenance of metabolic homeostasis. Furthermore, mEVs influence the production of SCFAs, which are critical in regulating microbial metabolism and optimizing energy and lipid metabolism.[46] High-fat diets are known to disrupt gut homeostasis by altering the composition and metabolic activity of gut microbiota, leading to the emergence of SCFA imbalanced state.[47,48] Furthermore, an increase in SCFAs induced by a high-fat diet was observed, which was subsequently partially restored by mEV intervention. This finding deviates from the conventional understanding of SCFA changes, highlighting the complexity of SCFA physiological functions.[49,50] SCFAs have a dual role: they enhance the intestinal barrier and suppress inflammation when produced by dietary fiber fermentation, but can disrupt intestinal homeostasis under high-fat-diet conditions due to abnormal fermentation and mucin-degrading bacteria proliferation.[49] Therefore, the role of mEVs in this study is to reduce the high-fat-diet-induced abnormal SCFA accumulation. This phenomenon aligns with recent obesity research and may suggest a combined mechanism at play. The high-fat diet disrupts gut microbiota balance, while mEVs optimize SCFA production through a triple mechanism that involves inhibiting pathogenic sources, promoting metabolic transformation, and restoring microbial balance. Collectively, these findings suggest that mEVs represent a novel intervention strategy for metabolic disorders such as obesity and diabetes, particularly through their beneficial effects on gut health.[51] Their efficacy likely depends on mEV cargo composition, though definitive mediators require future identification. Additionally, the potential of mEVs in drug delivery and immune modulation positions them as a promising platform for applications in biomedicine.

This study presents notable strengths and limitations. Its comprehensive methodology effectively investigates the effects of mEVs on thermogenesis and metabolic regulation in BAT, providing compelling evidence that mEVs enhance thermogenic activity and reduce lipid accumulation in mice on a high-fat diet. mEVs, as a noninvasive and natural intervention, harness the bioactive components in camel milk, offering a more sustainable and safer alternative for obesity treatment with fewer adverse effects. In contrast, GLP-1 receptor agonists such as liraglutide and semaglutide, while effective in controlling blood glucose and reducing body weight through enhanced insulin secretion and appetite suppression, are associated with substantial gastrointestinal, renal, and pancreatic side effects.[52,53] Thus, mEVs present a promising solution for metabolic health improvement, devoid of the common risks associated with pharmaceutical treatments, emphasizing their potential as a safer and more holistic approach to obesity management. However, our study was restricted to animal models and did not extend to clinical validation regarding the effects of mEVs in improving obesity. Additionally, the absence of EV cargo analysis (e.g., miRNAs, proteins) restricts mechanistic depth, as we cannot specify which components drive the observed activation of SOX4-EBF2 axis or microbiota remodeling. Additionally, while potential mechanisms of mEV action are suggested, further research is necessary to elucidate the specific signaling pathways involved. The absence of long-term follow-up raises questions about the sustainability of these effects and potential side effects associated with prolonged mEV administration.

https://doi.org/10.1021/acs.jafc.5c02577
J. Agric. Food Chem. 2025, 73, 21404−21421

■ ASSOCIATED CONTENT

Supporting Information

The Supporting Information is available free of charge at https://pubs.acs.org/doi/10.1021/acs.jafc.5c02577.

Supplementary Figures S1−S6, which complement the main manuscript (PDF)

Supplemental Table 1, which lists all primers used in this study (XLSX)

Uncropped Western blots (PDF)

■ AUTHOR INFORMATION

Corresponding Authors

Weihua Li − *Department of Cardiology, Xiamen Key Laboratory of Cardiac Electrophysiology, Xiamen Institute of Cardiovascular Diseases, The First Affiliated Hospital of Xiamen University, School of Medicine, Xiamen University, Xiamen 361003, China*; Email: liweihua@xmu.edu.cn

Jian Zhang − *School of Food Science and Technology, Jiangnan University, Wuxi 214122, China*; Email: 7210201081@stu.jiangnan.edu.cn

Authors

Shuai Wang − *State Key Laboratory of Cellular Stress Biology, Innovation Center for Cell Signaling Network and Engineering Research Center of Molecular Diagnostics of The Ministry of Education, School of Life Sciences, Xiamen University, Xiamen 361102 Fujian, China; Department of Cardiology, Xiamen Key Laboratory of Cardiac Electrophysiology, Xiamen Institute of Cardiovascular Diseases, The First Affiliated Hospital of Xiamen University, School of Medicine, Xiamen University, Xiamen 361003, China*; orcid.org/0009-0007-9880-1437

Shuting Liu − *State Key Laboratory of Cellular Stress Biology, Innovation Center for Cell Signaling Network and Engineering Research Center of Molecular Diagnostics of The Ministry of Education, School of Life Sciences, Xiamen University, Xiamen 361102 Fujian, China*

Ting He − *State Key Laboratory of Cellular Stress Biology, Innovation Center for Cell Signaling Network and Engineering Research Center of Molecular Diagnostics of The Ministry of Education, School of Life Sciences, Xiamen University, Xiamen 361102 Fujian, China*

Huanming Shen − *Shenzhen Institute of Advanced Technology, Chinese Academy of Science, Shenzhen 518055, China*

Chunli Mo − *Department of Cardiology, Xiamen Key Laboratory of Cardiac Electrophysiology, Xiamen Institute of Cardiovascular Diseases, The First Affiliated Hospital of Xiamen University, School of Medicine, Xiamen University, Xiamen 361003, China*

Yu Zhu − *State Key Laboratory of Cellular Stress Biology, Innovation Center for Cell Signaling Network and Engineering Research Center of Molecular Diagnostics of The Ministry of Education, School of Life Sciences, Xiamen University, Xiamen 361102 Fujian, China*

Wenlong Xie − *State Key Laboratory of Cellular Stress Biology, Innovation Center for Cell Signaling Network and Engineering Research Center of Molecular Diagnostics of The Ministry of Education, School of Life Sciences, Xiamen University, Xiamen 361102 Fujian, China*

Boan Li − *State Key Laboratory of Cellular Stress Biology, Innovation Center for Cell Signaling Network and Engineering Research Center of Molecular Diagnostics of The Ministry of Education, School of Life Sciences, Xiamen University, Xiamen 361102 Fujian, China*; orcid.org/0000-0002-2264-9295

Complete contact information is available at: https://pubs.acs.org/10.1021/acs.jafc.5c02577

Author Contributions

[⊥]SW and SL contributed equally to this study. SW, SL, and JZ designed the study, conducted data analysis, and drafted the manuscript. SW and SL performed the majority of the experiments. TH carried out bioinformatics analyses of RNA-seq data sets. HS, CM, YZ, and WX contributed to the mouse experiments. WL and BL supervised the project, revised the manuscript and provided funding. JZ served as the guarantor, had full access to all study data and takes responsibility for ensuring both data integrity and the accuracy of data analysis.

Funding

This work was supported by grants from the National Natural Science Foundation of China (82473163 to BL), Xiamen Municipal Bureau of Science and Technology (3502Z20224021 to WL), and Postdoctoral Fellowship Program of CPSF under Grant Number GZC20231412.

Notes

The authors declare no competing financial interest.

■ REFERENCES

(1) Donath, M. Y.; Shoelson, S. E. Type 2 diabetes as an inflammatory disease. *Nature Reviews Immunology* **2011**, *11* (2), 98−107.

(2) Gunasekar, S. K.; Xie, L.; Kumar, A.; Hong, J.; Chheda, P. R.; Kang, C.; Kern, D. M.; My-Ta, C.; Maurer, J.; Heebink, J.; Gerber, E. E.; Grzesik, W. J.; Elliot-Hudson, M.; Zhang, Y.; Key, P.; Kulkarni, C. A.; Beals, J. W.; Smith, G. I.; Samuel, I.; Smith, J. K.; Nau, P.; Imai, Y.; Sheldon, R. D.; Taylor, E. B.; Lerner, D. J.; Norris, A. W.; Klein, S.; Brohawn, S. G.; Kerns, R.; Sah, R. Small molecule SWELL1 complex induction improves glycemic control and nonalcoholic fatty liver disease in murine Type 2 diabetes. *Nat. Commun.* **2022**, *13* (1), 784−808.

(3) Hagberg, C. E.; Spalding, K. L. White adipocyte dysfunction and obesity-associated pathologies in humans. *Nat. Rev. Mol. Cell Biol.* **2024**, *25* (4), 270−289.

(4) Sethi, J. K.; Hotamisligil, G. S. Metabolic Messengers: tumour necrosis factor. *Nat. Metab* **2021**, *3* (10), 1302−1312.

(5) Chavakis, T.; Alexaki, V. I.; Ferrante, A. W., Jr. Macrophage function in adipose tissue homeostasis and metabolic inflammation. *Nature immunology* **2023**, *24* (5), 757−766.

(6) Wisse, B. E. The inflammatory syndrome: the role of adipose tissue cytokines in metabolic disorders linked to obesity. *Journal of the American Society of Nephrology: JASN* **2004**, *15* (11), 2792−2800.

(7) Luce, M.; Barba, C.; Yi, D.; Mey, A.; Roussel, D.; Bres, E.; Benoit, B.; Pastural, M.; Granjon, S.; Szelag, J. C.; Laville, M.; Arkouche, W.; Bouchara, A.; Nyam, E.; Fouque, D.; Soulage, C. O.; Koppe, L. Accumulation of natriuretic peptides is associated with protein energy wasting and activation of browning in white adipose tissue in chronic kidney disease. *Kidney international* **2020**, *98* (3), 663−672.

(8) Horvath, C.; Wolfrum, C. Feeding brown fat: dietary phytochemicals targeting non-shivering thermogenesis to control body weight. *Proceedings of the Nutrition Society* **2020**, *79* (3), 338−356.

(9) Wang, S.; He, T.; Luo, Y.; Ren, K.; Shen, H.; Hou, L.; Wei, Y.; Fu, T.; Xie, W.; Wang, P.; Hu, J.; Zhu, Y.; Huang, Z.; Li, Q.; Li, W.; Guo, H.; Li, B. SOX4 facilitates brown fat development and

maintenance through EBF2-mediated thermogenic gene program in mice. *Cell death and differentiation* **2025**, *32* (3), 447−465.
(10) Wang, W.; Seale, P. Control of brown and beige fat development. *Nat. Rev. Mol. Cell Biol.* **2016**, *17* (11), 691−702.
(11) Rajakumari, S.; Wu, J.; Ishibashi, J.; Lim, H. W.; Giang, A. H.; Won, K. J.; Reed, R. R.; Seale, P. EBF2 determines and maintains brown adipocyte identity. *Cell Metab* **2013**, *17* (4), 562−574.
(12) Cannon, B.; Nedergaard, J. Brown adipose tissue: function and physiological significance. *Physiol Rev.* **2004**, *84* (1), 277−359.
(13) Zhang, X.; Zhang, B.; Zhang, C.; Sun, G.; Sun, X. Trib1 deficiency causes brown adipose respiratory chain depletion and mitochondrial disorder. *Cell Death Dis* **2021**, *12* (12), 1098−1109.
(14) Wang, Y.; Gao, M.; Zhu, F.; Li, X.; Yang, Y.; Yan, Q.; Jia, L.; Xie, L.; Chen, Z. METTL3 is essential for postnatal development of brown adipose tissue and energy expenditure in mice. *Nat. Commun.* **2020**, *11* (1), 1648−1661.
(15) Du, H.; Shi, L.; Wang, Q.; Yan, T.; Wang, Y.; Zhang, X.; Yang, C.; Zhao, Y.; Yang, X. Fu Brick Tea Polysaccharides Prevent Obesity via Gut Microbiota-Controlled Promotion of Adipocyte Browning and Thermogenesis. *J. Agric. Food Chem.* **2022**, *70* (43), 13893−13903.
(16) Guo, L.; Yokoyama, W.; Chen, L.; Chen, M.; Zhong, F. Dynamic Hydration and Viscosity Control of Konjac Glucomannan Enhance Long-Term Antiobesity Effects by Reducing Food Intake in High-Fat-Diet-Fed Mice. *J. Agric. Food Chem.* **2024**, *72* (44), 24561−24575.
(17) Cani, P. D.; Van Hul, M. Gut microbiota in overweight and obesity: crosstalk with adipose tissue. *Nature reviews. Gastroenterology & hepatology* **2024**, *21* (3), 164−183.
(18) Chen, Y.; Gao, R.; Fang, J.; Ding, S. A review: Polysaccharides targeting mitochondria to improve obesity. *Int. J. Biol. Macromol.* **2024**, *277* (Pt 3), 134448−134460.
(19) Gao, F.; Wu, S.; Zhang, K.; Xu, Z.; Zhang, X.; Zhu, Z.; Quan, F. Goat Milk Exosomes Ameliorate Ulcerative Colitis in Mice through Modulation of the Intestinal Barrier, Gut Microbiota, and Metabolites. *J. Agric. Food Chem.* **2024**, *72* (42), 23196−23210.
(20) Qu, S.; Han, Y.; Liu, Y.; Zhu, J.; Acaroz, U.; Shen, J.; Zhu, K. Milk Exosomes Facilitate Oral Delivery of Drugs against Intestinal Bacterial Infections. *J. Agric. Food Chem.* **2022**, *70* (51), 16069−16079.
(21) Gao, H. N.; Hu, H.; Wen, P. C.; Lian, S.; Xie, X. L.; Song, H. L.; Yang, Z. N.; Ren, F. Z. Yak milk-derived exosomes alleviate lipopolysaccharide-induced intestinal inflammation by inhibiting PI3K/AKT/C3 pathway activation. *Journal of dairy science* **2021**, *104* (8), 8411−8424.
(22) Du, C.; Quan, S.; Zhao, Y.; Nan, X.; Chen, R.; Tang, X.; Xiong, B. Bovine milk-derived extracellular vesicles prevent gut inflammation by regulating lipid and amino acid metabolism. *Food Funct* **2023**, *14* (4), 2212−2222.
(23) Badawy, A. A.; El-Hofey, S. M.; Shaban, A. M.; Orif, S. E.; Uyanikgil, Y.; El-Magd, M. A. Camel milk extracellular vesicles/exosomes: a fascinating frontier in isolation and therapeutic potential. *Food & Function* **2025**, *16* (2), 344−365.
(24) Muttiah, B.; Law, J. X. Milk-derived extracellular vesicles and gut health. *Npj Science of Food* **2025**, *9* (1), 1−12.
(25) Al-zoreky, N. S.; Almathen, F. S. Using recombinant camel chymosin to make white soft cheese from camel milk. *Food Chem.* **2021**, *337*, 127994.
(26) Badawy, A. A.; El-Hofey, S. M.; Shaban, A. M.; Orif, S. E.; Uyanıkgil, Y.; El-Magd, M. A. Camel milk extracellular vesicles/exosomes: a fascinating frontier in isolation and therapeutic potential. *Food Funct* **2025**, *16* (2), 344−365.
(27) Gao, F.; Wu, S.; Zhang, K.; Xu, Z.; Zhang, X.; Zhu, Z.; Quan, F. Goat Milk Exosomes Ameliorate Ulcerative Colitis in Mice through Modulation of the Intestinal Barrier, Gut Microbiota, and Metabolites. *J. Agric. Food Chem.* **2024**, *72* (42), 23196−23210.
(28) Zhang, J.; Huang, Y.; Bai, N.; Sun, Y.; Li, K.; Ruan, H.; Yan, B.; Hu, J.; Zhang, N.; Zhang, H.; Chen, W.; Fan, D. Spirulina platensis components mitigate bone density loss induced by simulated microgravity: A mechanistic insight. *Food Chem.* **2025**, *463*, 141361−141374.
(29) De Siqueira, M. K.; Li, G.; Zhao, Y.; Wang, S.; Ahn, I. S.; Tamboline, M.; Hildreth, A. D.; Larios, J.; Schcolnik-Cabrera, A.; Nouhi, Z.; Zhang, Z.; Tol, M. J.; Pandey, V.; Xu, S.; O'Sullivan, T. E.; Mack, J. J.; Tontonoz, P.; Sallam, T.; Wohlschlegel, J. A.; Hulea, L.; Xiao, X.; Yang, X.; Villanueva, C. J. PPARγ-dependent remodeling of translational machinery in adipose progenitors is impaired in obesity. *Cell Rep* **2024**, *43* (12), 114945−114971.
(30) Reinhardt, T. A.; Lippolis, J. D.; Nonnecke, B. J.; Sacco, R. E. Bovine milk exosome proteome. *J. Proteomics* **2012**, *75* (5), 1486−1492.
(31) Samuel, M.; Fonseka, P.; Sanwlani, R.; Gangoda, L.; Chee, S. H.; Keerthikumar, S.; Spurling, A.; Chitti, S. V.; Zanker, D.; Ang, C. S.; Atukorala, I.; Kang, T.; Shahi, S.; Marzan, A. L.; Nedeva, C.; Vennin, C.; Lucas, M. C.; Cheng, L.; Herrmann, D.; Pathan, M.; Chisanga, D.; Warren, S. C.; Zhao, K.; Abraham, N.; Anand, S.; Boukouris, S.; Adda, C. G.; Jiang, L.; Shekhar, T. M.; Baschuk, N.; Hawkins, C. J.; Johnston, A. J.; Orian, J. M.; Hoogenraad, N. J.; Poon, I. K.; Hill, A. F.; Jois, M.; Timpson, P.; Parker, B. S.; Mathivanan, S. Oral administration of bovine milk-derived extracellular vesicles induces senescence in the primary tumor but accelerates cancer metastasis. *Nat. Commun.* **2021**, *12* (1), 3950−3965.
(32) Claflin, K. E.; Flippo, K. H.; Sullivan, A. I.; Naber, M. C.; Zhou, B.; Neff, T. J.; Jensen-Cody, S. O.; Potthoff, M. J. Conditional gene targeting using UCP1-Cre mice directly targets the central nervous system beyond thermogenic adipose tissues. *Mol. Metab* **2022**, *55*, 101405−101412.
(33) Harms, M. J.; Ishibashi, J.; Wang, W.; Lim, H. W.; Goyama, S.; Sato, T.; Kurokawa, M.; Won, K. J.; Seale, P. Prdm16 is required for the maintenance of brown adipocyte identity and function in adult mice. *Cell Metab* **2014**, *19* (4), 593−604.
(34) Wu, L.; Xia, M.; Duan, Y.; Zhang, L.; Jiang, H.; Hu, X.; Yan, H.; Zhang, Y.; Gu, Y.; Shi, H.; Li, J.; Gao, X.; Li, J. Berberine promotes the recruitment and activation of brown adipose tissue in mice and humans. *Cell Death Dis* **2019**, *10* (6), 468−485.
(35) Ueta, C. B.; Fernandes, G. W.; Capelo, L. P.; Fonseca, T. L.; Maculan, F. D.; Gouveia, C. H.; Brum, P. C.; Christoffolete, M. A.; Aoki, M. S.; Lancellotti, C. L.; Kim, B.; Bianco, A. C.; Ribeiro, M. O. β(1) Adrenergic receptor is key to cold- and diet-induced thermogenesis in mice. *J. Endocrinol* **2012**, *214* (3), 359−365.
(36) Lee, H. J.; Lee, J.; Yang, M. J.; Kim, Y. C.; Hong, S. P.; Kim, J. M.; Hwang, G. S.; Koh, G. Y. Endothelial cell-derived stem cell factor promotes lipid accumulation through c-Kit-mediated increase of lipogenic enzymes in brown adipocytes. *Nat. Commun.* **2023**, *14* (1), 2754−2771.
(37) Stine, R. R.; Shapira, S. N.; Lim, H. W.; Ishibashi, J.; Harms, M.; Won, K. J.; Seale, P. EBF2 promotes the recruitment of beige adipocytes in white adipose tissue. *Mol. Metab* **2016**, *5* (1), 57−65.
(38) Yao, L.; Cui, X.; Chen, Q.; Yang, X.; Fang, F.; Zhang, J.; Liu, G.; Jin, W.; Chang, Y. Cold-Inducible SIRT6 Regulates Thermogenesis of Brown and Beige Fat. *Cell Rep* **2017**, *20* (3), 641−654.
(39) Wang, S.; He, T.; Luo, Y.; Ren, K.; Shen, H.; Hou, L.; Wei, Y.; Fu, T.; Xie, W.; Wang, P.; Hu, J.; Zhu, Y.; Huang, Z.; Li, Q.; Li, W.; Guo, H.; Li, B. SOX4 facilitates brown fat development and maintenance through EBF2-mediated thermogenic gene program in mice. *Cell Death Differ.* **2025**, *32* (3), 447−465.
(40) Shen, H.; He, T.; Wang, S.; Hou, L.; Wei, Y.; Liu, Y.; Mo, C.; Zhao, Z.; You, W.; Guo, H.; Li, B. SOX4 promotes beige adipocyte-mediated adaptive thermogenesis by facilitating PRDM16-PPARγ complex. *Theranostics* **2022**, *12* (18), 7699−7716.
(41) Hu, J.; Wang, Z.; Tan, B. K.; Christian, M. Dietary polyphenols turn fat "brown": A narrative review of the possible mechanisms. *Trends in Food Science & Technology* **2020**, *97*, 221−232.
(42) Quan, L. H.; Zhang, C.; Dong, M.; Jiang, J.; Xu, H.; Yan, C.; Liu, X.; Zhou, H.; Zhang, H.; Chen, L.; Zhong, F. L.; Luo, Z. B.; Lam, S. M.; Shui, G.; Li, D.; Jin, W. Myristoleic acid produced by enterococci reduces obesity through brown adipose tissue activation. *Gut* **2020**, *69* (7), 1239−1247.

(43) del Pozo-Acebo, L.; Lopez de las Hazas, M-C; Tome-Carneiro, J.; Gil-Cabrerizo, P.; San-Cristobal, R.; Busto, R.; Garcia-Ruiz, A.; Davalos, A. Bovine Milk-Derived Exosomes as a Drug Delivery Vehicle for miRNA-Based Therapy. *Int. J. Mol. Sci.* **2021**, *22* (3), 1105−1122.
(44) Du, C.; Wang, K.; Zhao, Y.; Nan, X.; Chen, R.; Quan, S.; Xiong, B. Supplementation with Milk-Derived Extracellular Vesicles Shapes the Gut Microbiota and Regulates the Transcriptomic Landscape in Experimental Colitis. *Nutrients* **2022**, *14* (9), 1808−1823.
(45) Zhao, X. Y.; Zhao, B. C.; Li, H. L.; Liu, Y.; Wang, B.; Li, A. Q.; Zeng, T. S.; Hui, H. X.; Sun, J.; Cikes, D.; Gheldof, N.; Hager, J.; Mi, J. X.; Laybutt, D. R.; Deng, Y. Y.; Shi, Y. C.; Neely, G. G.; Wang, Q. P. MTCH2 Suppresses Thermogenesis by Regulating Autophagy in Adipose Tissue. *Adv. Sci. (Weinh)* **2025**, *12* (17), e2416598.
(46) Xu, Y.; Zhu, Y.; Li, X.; Sun, B. Dynamic balancing of intestinal short-chain fatty acids: The crucial role of bacterial metabolism. *Trends in Food Science & Technology* **2020**, *100*, 118−130.
(47) Jamar, G.; Ribeiro, D. A.; Pisani, L. P. High-fat or high-sugar diets as trigger inflammation in the microbiota-gut-brain axis. *Crit Rev. Food Sci. Nutr* **2021**, *61* (5), 836−854.
(48) Liu, Y.; Yang, K.; Jia, Y.; Shi, J.; Tong, Z.; Fang, D.; Yang, B.; Su, C.; Li, R.; Xiao, X.; Wang, Z. Gut microbiome alterations in high-fat-diet-fed mice are associated with antibiotic tolerance. *Nature microbiology* **2021**, *6* (7), 874−884.
(49) Du, L.; Lü, H.; Chen, Y.; Yu, X.; Jian, T.; Zhao, H.; Wu, W.; Ding, X.; Chen, J.; Li, W. Blueberry and Blackberry Anthocyanins Ameliorate Metabolic Syndrome by Modulating Gut Microbiota and Short-Chain Fatty Acids Metabolism in High-Fat Diet-Fed C57BL/6J Mice. *J. Agric. Food Chem.* **2023**, *71* (40), 14649−14665.
(50) Gui, L.; Wang, S.; Wang, J.; Liao, W.; Chen, Z.; Pan, D.; Xia, H.; Sun, G.; Tian, S. Effects of forsythin extract in Forsythia leaves on intestinal microbiota and short-chain fatty acids in rats fed a high-fat diet. *Food Science and Human Wellness* **2024**, *13* (2), 659−667.
(51) Li, D.; Yao, X.; Yue, J.; Fang, Y.; Cao, G.; Midgley, A. C.; Nishinari, K.; Yang, Y. Advances in Bioactivity of MicroRNAs of Plant-Derived Exosome-Like Nanoparticles and Milk-Derived Extracellular Vesicles. *J. Agric. Food Chem.* **2022**, *70* (21), 6285−6299.
(52) Long, B.; Pelletier, J.; Koyfman, A.; Bridwell, R. E. GLP-1 agonists: A review for emergency clinicians. *Am. J. Emerg Med.* **2024**, *78*, 89−94.
(53) Andreadis, P.; Karagiannis, T.; Malandris, K.; Avgerinos, I.; Liakos, A.; Manolopoulos, A.; Bekiari, E.; Matthews, D. R.; Tsapas, A. Semaglutide for type 2 diabetes mellitus: A systematic review and meta-analysis. *Diabetes Obes Metab* **2018**, *20* (9), 2255−2263.

https://doi.org/10.1021/acs.jafc.5c02577
J. Agric. Food Chem. 2025, 73, 21404−21421